2015

Development of the ℓ^2 ω Delayed Detached Eddy Simulation model with dynamically computed constant

Zifei Yin
Iowa State University

Development of the $\ell^2\omega$ Delayed Detached Eddy Simulation model with dynamically computed constant

by

Zifei Yin

A thesis submitted to the graduate faculty

in partial fulfillment of the requirements for the degree of

MASTER OF SCIENCE

Major: Aerospace Engineering

Program of Study Committee:

Paul A. Durbin, Major Professor

Ping Lu

Jonathan Regele

Iowa State University

Ames, Iowa

2015

DEDICATION

I would like to dedicate this thesis to my parents and sister without whose support I would not have been able to complete this work.

TABLE OF CONTENTS

LIST OF TABLES

LIST OF FIGURES

ACKNOWLEDGEMENTS

I would like to take this opportunity to express my thanks to those who helped me with various aspects of conducting research and the writing of this thesis.

I would like to thank my major professor, Dr. Paul Durbin, for guiding me though the mist of this research field. I would also like to thank my friends and family for their loving guidance and financial assistance during the writing of this work.

Also I would like to thank Dr. Ping Lu and Dr. Jonathan Regele for helping me further understand my research by raising questions with deep insight in the oral exam.

ABSTRACT

The current work puts forth an implementation of a dynamic procedure to locally compute the value of the model constant C_{DES} , as used in the eddy simulation branch of Delayed Detached Eddy Simulation (DDES). Former DDES formulations [P. R. Spalart et al., A new version of detached-eddy simulation, resistant to ambiguous grid densities, Theor. Comput. Fluid Dyn. 20, 181 (2006); M. S. Gritskevich et al., Development of DDES and IDDES formulations for the $k-\omega$ shear stress transport model, Flow, Turbul. Combust. 88, 431 (2012)] are not conducive to the implementation of a dynamic procedure due to uncertainty as to what form the eddy viscosity expression takes in the eddy simulation branch. However, a recent, alternate formulation [K. R. Reddy et al., A DDES model with a Smagorinsky-type eddy viscosity formulation and log-layer mismatch correction, Int. J. Heat Fluid Flow 50, 103 (2014)] casts the eddy viscosity in a form that is similar to the Smagorinsky, LES (Large Eddy Simulation) sub-grid viscosity. The resemblance to the Smagorinsky model allows the implementation of a dynamic procedure similar to that of Lilly [D. K. Lilly, A proposed modification of the Germano subgrid-scale closure method, Phys. Fluids A 4, 633 (1992)]. A limiting function is proposed which constrains the computed value of C_{DES} , depending on the fineness of the grid and on the computed solution. In addition to the dynamic procedure, influence of inflow condition is also explored in this work.

CHAPTER 1. INTRODUCTION

For industrial applications of turbulence simulation, Reynolds Averaged Navier Stokes (RANS) models are widely used, but they can produce insufficiently accurate results for complex geometries. Though more accurate, Large Eddy Simulation(LES) is not practical in industry in upcoming decades because of its high demand on computing resources. Detached Eddy Simulation (DES) was proposed to fill the gap between RANS and LES with much more accuracy but manageable increase of cost. It is a modification of a RANS model, which switches to a subgrid scale formulation in regions where the turbulence scales are large enough for LES calculation. The original DES formulation suffers from Grid Induced Separation (GIS) and Log-Layer Mismatch (LLM). Those shortcomings lead to the development of Delayed DES (DDES) to prevent GIS and to Improved DDES (IDDES) to alleviate LLM. IDDES introduces a lot of empiricism. Recently our group has proposed an alternative DDES formulation that alleviates LLM. The eddy viscosity is formulated in a similar way to the subgrid viscosity in the Smagorinsky model. The need of adjusting the constant in the Smagorinsky model is inherited in our DDES model. That leads naturally to the current work, allowing model constant to be computed via a dynamic procedure: stresses are computed from the resolved scales via a test filter, and the constant optimizes a fit between modeled and resolve stresses. A limiting function is proposed to set constrains on the computed model constant, depending on the mesh resolution and turbulence scales. Tests of the the dynamic procedure are made on benchmark cases.

CHAPTER 2. REVIEW OF LITERATURE

In simulation of turbulent flow, it has always been a trade off between computing power and solution accuracy especially for industrial application. Reynolds Averaged Navier Stokes (RANS) models separate flow character into time averaged and fluctuations parts. Time averaged flow is solved and fluctuation part is modeled. Those models have been widely used in industry but sometimes are insufficiently accurate, especially for flow over complex geometries. Large Eddy Simulation (LES) resolves a large portion of turbulent motions which improves accuracy but also brings extraordinary demand for computing power. Direct Numerical Simulation (DNS), which resolves all the turbulent motions, is far beyond application level in industry. Detached Eddy Simulation, as one kind of the Hybrid RANS and LES branch, was proposed to predict turbulent flows at high Reynolds number with better accuracy than RANS in massively separated flow without exceeding manageable computing power.

2.1 Physical Aspect of Turbulence

2.1.1 The Kolmogorov's Hypotheses

$$\eta = (\frac{\nu^3}{\epsilon})^{\frac{1}{4}} \tag{2.1}$$

There are three hypotheses from Kolmogorov's theory [Kolmogorov (1941)]. Kolmogorov's hypothesis of local isotropy assumes that at sufficiently high Reynolds number, the small scale turbulent motions are statistically isotropic. Kolmogorov's first similarity hypothesis states that in every turbulent flow at sufficiently high Reynolds number, the statistics of the small scale motions have a universal form that is uniquely determined by dissipation ϵ and molecular viscosity ν, as equation 2.1 Kolmogorov's second similarity hypothesis states that in every

turbulent flow at sufficiently high Reynolds number, the statistics of the motions $\ell_0 >> \ell >> \eta$ have a universal form that is uniquely determined by dissipation ϵ but independet of molecular viscosity ν.

2.1.2 The Turbulence Energy Spectrum

Turbulent flow contains a wide range of scales of motion and energy transferring between scales. The energy spectrum function of wave number $E(\kappa)$ is a straightforward way to examine the distribution of energy over scales. The energy transfer can be divided into three principal portions based on scales. The largest, named as energy containing range, doesn't have a universal character. It is based on flow configurations such as boundary condition. The smallest scales are in the dissipation range, which is determined by the dissipation and molecular viscosity. Scales between the energy containing range and the dissipation range belong to the inertial subrange. Those scales, that only depends on the dissipation, are still in universal equilibrium.

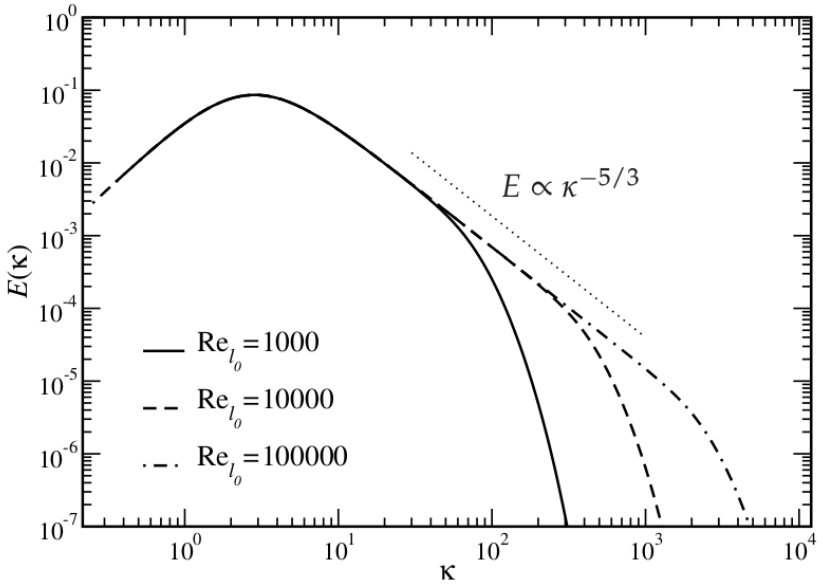

Figure 2.1: Energy spectrum for varying Reynolds number [Pope (2000)]

Based on the second Kolmogorov hypothesis, within the inertial subrange, it is found that $E(\kappa) \propto \kappa^{-5/3}$ [Pope (2000)]. This is a universal form which only depends on the Reynolds number for isotropic turbulence.

2.1.3 Universality of Boundary Layer Profiles

Although flow characteristics are determined by flow configurations, boundary layer profile has some universal properties termed as law of the wall. The law of the wall is not totally independent of flow outside boundary layer, for example the outermost region of flate plate boundary layer and fully developed channel flow can be different but the inside region quite similar.

Law of the wall is based on nondimensionalizing the boudnary layer profile by plus units, $^+$. Which is based on wall shear stress, τ_w. For example, velocity is normalized by wall friction velocity which is defined as equation 2.2.

$$u_\tau = \sqrt{\frac{\tau_w}{\rho}} \tag{2.2}$$

Normalized velocity u^+ is a function of normalized wall distance y^+ and this function is universal. And flow characteristics are related to such normalized wall distance. Such as with in viscous sublayer ($y^+ < 5$), the role of Reynolds shear stress is negligible and the molecular viscosity is dominant. Thus, approximately $U^+ = y^+$ describes the velocity profile here. From $y^+ > 40$ to central of a funlly developed channel or 0.2δ of flat plate boudnary layer is called the log-layer. In this region molecular viscosity is negligible compared to Reynolds stress. The log law applies here as equation 2.3. The constant κ is the vol Karman constant which is usually about 0.41. B is approximated 5.2 by curve fitting of experimental data. Region between log-layer and viscos sublayer is the buffer layer, with $5 < y^+ < 40$.

$$U^+ = \frac{1}{\kappa} ln y^+ + B \tag{2.3}$$

2.2 Simulation and Modeling of Turbulence

There are three main kinds of methods of solving Navier-Stokes equations, Reynolds Averaged Navier Stokes (RANS), Large Eddy Simulation (LES) and Direct Numerical Simulation (DNS). RANS is the cheapest and is ready for industrial use since the 1990s. LES consumes a lot more CPU power and its scaling with Reynolds number makes it prohibitive to be used

in the industry a few decades, not even mention DNS. Hybrid RANS/LES improves accuracy but also reduces demand on computing power which can be a possible approach to fill the gap between RANS and LES.

2.2.1 Reynolds Averaged Navier Stokes

Reynolds Averaged Navier Stokes models solve time averaged flow field. Its idea is built on ensemble average and Reynolds decomposition. The instantaneous field is broken down into time averaged field and fluctuation field. The fluctuation field is being modeled and the time averaged field is solved in Reynolds Averaged Navier Stokes equations. Extra equations are established to close the set of equations. Usually there are a bunch of empirical constants in a RANS model that are calibrated with simple turbulent flows such as decaying isotropic turbulence. Those characters make a RANS model incapable of providing satisfactory results for complex geometries. Although Unsteady RANS has been developed and makes RANS possible to capture some unsteady motion in a turbulent flow. It is hard to say it is physically sound since it is still based on statistical time averaging of the flow field.

There are two main kinds of RANS models. The first is constructed on Boussinesq eddy viscosity hypothesis [Pope (2000)] and can be written as equation 2.4. Extra one or two equations are used to solve the eddy viscosity (ν_T) to incorporate the time averaged N-S equation. One equation models like Spalart-Allmaras model and two equation models such as $k-\epsilon$ and $k-\omega$ all fall in this kind.

$$-\tau_{ij} + \frac{1}{3}\tau_{kk} = 2\nu_T S_{ij} \tag{2.4}$$

The other kind the Reynolds Stress Models (RSM). Though not as widely used as eddy viscosity models, these models can sometimes better predict the Reynolds stress because it can be more elaborately presented. RSM models can respond to flow characters like buoyancy, rotation and curvature. However, due to the formulation of dissipation terms, in some flow its performance is as bad as eddy viscosity models. In those models, six unknown components in Reynolds stress are being solved which lead to complexity and insufficient robustness.

The baseline of two transport equation models is to solve for turbulent kinetic energy (k) and turbulent dissipation (ϵ), which is the standard $k-\epsilon$ model [Launder and Sharma (1974)]. The $k-\epsilon$ model performs poorly for complex flows involving severe pressure gradient, separation, strong streamline curvature. Near wall behavior of the eddy viscosity is wrong so it requires a damping function or extra equations. $k-\epsilon$ model is not as sensitive as $k-\omega$ model to inflow conditions.

Another classic two equation eddy viscosity is Wilcox's $k-\omega$ model [Wilcox (1993)]. It defines eddy viscosity as equation 2.5. Transport equations for turbulent kinetic energy and specific dissipationj rate is defines in equation 2.6 and equation 2.7. For the near wall behavior, $k-\omega$ model doesn't predict correctly k profile but approximately correct ν_T profile, which requires mesh resolution near the wall. Which means $k-\omega$ model does not require any damping function near wall. Compare with other classic eddy viscosity models, the $k-\omega$ model has superior performance for wall bounded boundary layer, free shear and low Reynolds number flows. It is more appropriate for complex boundary layer flows than $k-\epsilon$ model under adverse pressure gradient and separation. However, it typically predicts excessive and early separation. It also can predict premature transition.

$$\nu_T = k/\omega \tag{2.5}$$

$$\frac{Dk}{Dt} = \tau_{ij}\frac{\partial U_i}{\partial x_i} - C_\mu k\omega + \frac{\partial}{\partial_j}[(\nu + \sigma_k(k/\omega))\frac{\partial k}{\partial x_i}] \tag{2.6}$$

$$\frac{D\omega}{Dt} = \alpha\frac{\omega}{k}\tau_{ij}\frac{\partial U_i}{\partial x_i} - C_{\omega 2}\omega^2 + \frac{\partial}{\partial_j}[(\nu + \sigma_\omega(k/\omega))\frac{\partial \omega}{\partial x_i}] \tag{2.7}$$

The $k-\omega$ model can be integrated to wall but is too sensitive to free stream boundary condition. The $k-\epsilon$ model is more robust in the free stream. This results in the SST model formulation. It combines the original Wilcox $k-\omega$ model for near walls regions and the standard $k-\epsilon$ model away from the walls with a blending function. The use of $k-\omega$ in near wall region allows the SST model to be used as low-Re model without wall function. And the eddy viscosity formulation is modified to take the transport effect of the principle turbulent shear stress into account.

2.2.2 Large Eddy Simulation

As mentioned in section 2.1.1 that the small scales in a turbulent flow are universal and only depends on the Reynolds number. The principal operation in Large Eddy Simulation (LES) is low pass filtering. The operation is applied to the Navier-Stokes equations to filter out small scales of the solution. In another word, the universal small scales are modeled and the rest are resolved. A large portion of turbulence being resolved provides better fidelity than alternative approaches such as RANS. However, such portion of resolved turbulent puts a strict limit on the upper bound on the cut-off length. That requirement makes wall resolved LES extremely expensive for wall bounded flows.

The modeled part is unresolved and the scales are smaller than cutoff filter width. It is termed as subgrid stress. The filtering process is based on how to model the subgrid stress. Sometimes the subgrid stress doesn't have a high correlation with actual filtered flow field of DNS solution. As long as it predicts appropriate time averaged solution, there is some freedom in modeling the subgrid stress. There are two kinds of modeling, one is similar to the RANS idea to use subgrid viscosity like Smagorinsky model, the other is based on flow structure like the similarity model [Bardina et al. (1980)]. Linear combination of those two kinds also exists, which can have higher correlation with actual stress than Smagorinsky model and more proper dissipation than similarity model. Also there are other ways like implicit-LES, which uses numerical dissipation to replace the role of dissipation brought by subgrid stress.

The widely used Smagorinsky model [Smagorinsky (1963)] was based on the idea of the Prandtl mixing length theory. The length scale is defined as $C_s\Delta$ where Δ is the cube root of local cell volume and C_s is a model constant. The subgrid viscosity is defined as equation 2.8.

$$\nu_{sgs} = (C_s\Delta)^2 |S| \tag{2.8}$$

The model constant C_S in Smaogrinsky is not a universal constant. It needs to be adapted according to flow. For decaying isotropic turbulence, C_s is found to be approximately 0.17. For free shear flows a near zero value will be best suited. It is also found that the Smagorinsky model is too dissipative near wall. Either a damping function or the dynamic procedure [Lilly (1992)] is required to reduce the model constant near wall.

The dynamic procedure on Smagorinsky model is proposed by Germano et al. (1991), then modified by Lilly (1992) based on least square minimization. The formulation is listed in equation 2.9. However, the evaluated C_s^2 is unstable and sometimes become negative. In practice the negative evaluated C_s^2 values are clipped out for the sake of numerical stability.

$$C_s^2 = \frac{L_{ij}M_{ij}}{2M_{ij}M_{ij}} \tag{2.9}$$

$$dev(L_{ij}) = dev(T_{ij} - \hat{\tau_{ij}}) = dev(-\widehat{\bar{u}_i\bar{u}_j} + \hat{\bar{u}}_i\hat{\bar{u}}_j) \tag{2.10}$$

$$M_{ij} = \hat{\Delta}^2|\hat{\bar{S}}|\hat{\bar{S}}_{ij} - \Delta^2\widehat{|\bar{S}|\bar{S}_{ij}} \tag{2.11}$$

$dev(L_{ij})$ here means the trace free part of L_{ij}. C_s^2 is also very unstable both in time and space from such dynamic procedure. For flow with at least one homogeneous direction, C_s^2 is recommended to be averaged over those directions. For example, in fully developed channel flow, C_s^2 is evaluated over spanwise and streamwise. Lagrangian averaging, meaning C_s^2 is averaged over fluid pathline, is also proposed [Meneveau et al. (1996)]. A new time constant is brought in by such lagrangian averaging, and it seems not to be a true constant. As a result another dynamic procedure [Verma and Mahesh (2012)] for such evaluating time constant is introduced but is not easy to implement in CFD code.

There are also some other subgrid eddy viscosiy formulations declear to be able to get rid of dynamic proceudre. For example, the Wall-Adapting Local Eddy-Viscosity (WALE) model [Ducros et al. (1998)], defines a inverse time scale, corresponding to $|S|$ in Smagorinsky model, that is computed based on flow structure. The adjusting of eddy viscosity according to flow is carried out by adjusting this inverse time scale rather than length scales.

2.2.3 Direct Numerical Simulation

Direct Numerical Simulation (DNS), the most demanding method, doesn't model any scale of motion. All scales, both spatial and temporal, are resolved by directly solving Navier Stokes equations. It is expect to be the most accurate method. Kolmogorov scaling makes the total number of grid scale like $Re^{\frac{9}{4}}$. As a result, DNS is only practical on low Reynolds number cases like channel flow at Re_τ around several hundreds. DNS has enought resolution on the flow field and when adequate numerical scheme and appropriate boundary condition are used.

There is no empirism in DNS so it can be regarded accurate. Constants in other more empirical methods like LES and RANS can be tuned according to comparison with DNS data on simple flows. Due to its high resolution, DNS is also a powerful tool in fundamental research, which sometimes doesn't have enough experimental data. In another word, DNS can provide some data that can not be measured in experiments.

2.2.4 Hybrid RANS/LES Methods

Hybrid RANS/LES method contains a wide range of possible formulations. DES is one kind of those hybrid model which is based solely on a single RANS model. There are also other formulations like applying hybrid filters to represent Reynolds Averaged operation and the LES filter [Rajamani and Kim (2010)]. Linear interpolation of RANS and LES is also tried [Walters et al. (2013)]. It is based on linear interpolation on Reynolds stress and subgrid stress. Also, Zonal-DES is also proposed. Zonal-DES approach is not really an DES formulation because it is basically applying two different models in pre-specified regions. Interface between LES and RANS in such zonal approach is troublesome. There are also Wall Modeling LES (WMLES) formulations to reduce the demands on CPU power because near wall resolution requirement is the most grid consuming part. Wall models are used to provide the velocity profile near the wall based on universal boundary layer profile and the LES models are applied outside the near wall region. Very Large Eddy Simulation and Embedded LES also fall in this scope.

2.3 Detached Eddy Simulation

Detached Eddy Simulation is a hybrid RANS/LES model which is constructed based on a single RANS formulation with modifications on length scales. It is designed to improve predictions on massive separated flow without increasing too much grid resolution requirement.

2.3.1 DES97

The first DES model, which was proposed by Spalart et al. (1997), is based on the Spalart Allmaras model [Spalart and Allmaras (1992)]. The modification is to replace the length scale

definition in the dissipation term in the $\tilde{\nu}$ equation. The original length scale is the wall distance. It is replaced by equation 2.12

Where d is still the wall distance. $\Delta = max(\Delta X, \Delta Y, \Delta Z)$ which is the maximum local cell spacing. C_{DES} is a model constant. In the near wall region, because wall distance is smaller than the cell spacing, $\tilde{d}$ equals to wall distance which is the same as Spalart Allmaras RANS model. When away from the wall, switching to cell spacing is used to enhance dissipation in $\tilde{\nu}$ equation to reduce eddy viscosity which allows unsteadiness to be developed.

$$\tilde{d} = min(d, C_{DES} * \Delta) \tag{2.12}$$

The original DES formulation has two fundamental flaws. On ambiguous grids Grid Induced Separation (GIS) was observed which is due to Modeled Stress Depletion (MSD). This is because on those grids the model switches from RANS to LES too early that even it is in the eddy simulation region, there is no enough turbulence resolved. Insufficient total stress will cause flow separation early than where RANS model predicted. The second problem, Log-Layer Mismatch (LLM), is also associated with total stress distribution. On the non-dimensional velocity profile, there are two log-layer predicted by RANS and LES, but they do not align with each other. This is because there is not enough total stress in the RANS/LES interface, velocity gradient need to be increased in order to balance the momentum transfer.

2.3.2 GIS and DDES

Figure 2.2 shows the basic idea of what a grid induced separation is like. The DES model predicts a much earlier separation location than the RANS model. It usually happens on ambiguous grid where the grid spacing is comparable to boundary layer thickness. Switching from RANS to LES doesn't necessary mean that the local grid resolution is fine enough to resolve accurate LES content. LES content develops too slow to fullfill the decreased portion of modeled stress. Which is termed as Modeled Stress Depletion. Such mechanism results in insufficient total stress at the RANS/LES interface. Earlier separation location and other defects can be expected from modeled stress depletion, especially under adverse pressure.

Figure 2.3 shows what kind of mesh is ambiguous for DES. The first mesh is what DES was originally designed for. It is a boundary layer grid with wall-parallel spacing excess of the boundary thickness. For the DES97 formulation, the entire boundary layer is solved by RANS. The third grid is fine enough for an LES simulation, though the RANS/LES switching location is inside the boundary layer, the mesh after the switching is actually fine enough to resolve enough Reynolds stress, which won't cause GIS. The second mesh with wall-parallel spacing near the magnitude of boundary layer thickness is in fact troublesome. The switching occurs within the boundary layer but the mesh is not good enough to resolve enough Reynolds stress. With the reduction of modeled stress, the total stress is underpredicted which causes GIS in figure 2.2.

In Delayed Detached Eddy Simulation, a shielding function is applied on DES model to ensure eddy simulation is not applied to too close to wall [Spalart et al. (2006)]. The shielding function delays switching from RANS length scale to LES length scale in some grid and makes the switch smoother. The first shielding processe was proposed by Menter and Kuntz (2004), in which the DES limiter is disabled as long as the flow is recognized as a boundary layer. The detection of boundary layer is achieved by the SST F_2 function. After that, a generic formulation of shielding function was proposed [Spalart et al. (2006)]. This generic shielding function can apply on any RANS model. The formulation for a DDES model with be like equation 2.13

$$\ell_{DDES} = \ell_{RANS} - f_d * max(0, \ell_{RANS} - \ell_{LES}) \tag{2.13}$$

2.3.3 LLM and IDDES

There are also some efforts trying to use a DES model in WMLES simulations on channel flow. The concept of using RANS as wall model and LES in other region was suggested long before DES. DES gives a simpler formulation to achieve this within a single model. There are early efforts in trying to use DES as WMLES in channel flow [Nikitin et al. (2000)]. Although it shows promising results in that high Reynolds number cases can be simulated with low increase in computational cost, there are key flaws. The result shows significant log layer mismatch. An

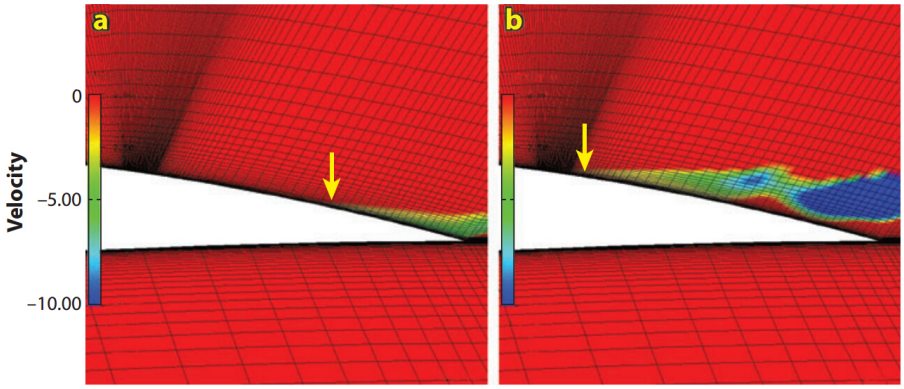

Figure 2.2: Grid Induced Separation, (a) RANS, (b)DES., figure taken from Menter and Kuntz (2004)

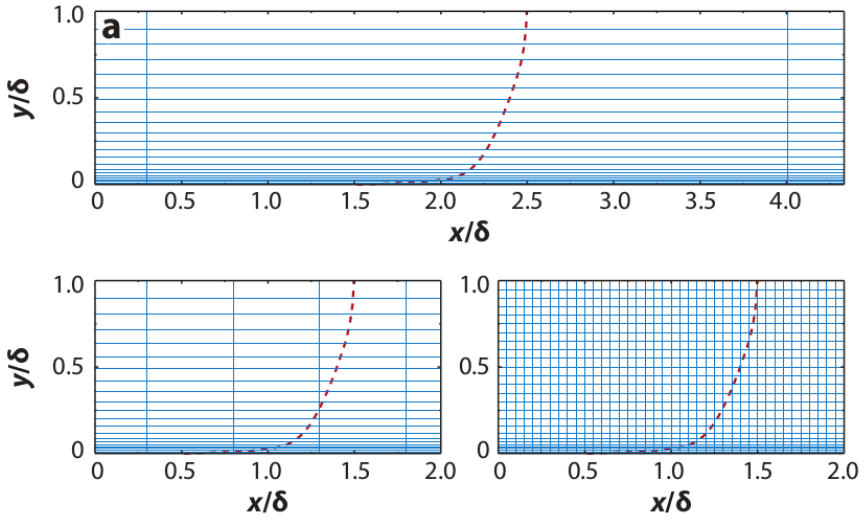

Figure 2.3: Different grid distribution for DES, figure taken from Spalart et al. (2006)

underpredict of skin friction coefficient by approximately 15% is observed in channel flow cases. The velocity wall normal gradient at the RANS/LES interface is too high that the log layers predicted by RANS and LES have nearly the same slope but different intercept. Refining the grid actually transfers this high gradient area near the wall.

The argument [Baggett (1998)] is that those unphysical, elongated wall streaks in the RANS region cause a de-correlation between streamwise and wall-normal fluctuations that must be compensated by a higher velocity gradient to balance the streamwise momentum. The discrepancy between the log-law intercepts in the inner and outer part of log-layer is caused by the transition between RANS and LES regions. In this region, the eddy viscosity is already reduced

significantly below normal value expected from pure RANS model. But the flow is more like URANS rather than an LES without enough smaller scales to fill the required Reynolds stress. In a gradient diffusion sense, the only way to reach the equilibrium value of shear stress is by the velocity gradient increase to balance the eddy viscosity decrease.

The shielding function in DDES only fixes GIS which leaves LLM still an open question. In Travin et al. (2006), length scale for the Spalart Allmaras DES model was changed from maximum local cell spacing to cubic root of cell volume. The rationale of changing the LES length scale is based on the suggestion of facilitating the generation of Reynolds stress generating structures Piomelli et al. (2002). The IDDES formulation of Shur et al. (2008) is quite ambitious. For one reason the IDDES formulation is aimed to solve LLM and GIS, for another reason both WMLES and nature DES capabilities are expected. In addition to modified cell spacing definition, wall distance is also taken account. The modification tends to depress near the wall and give it a steep variation, which stimulates instabilities, boosting the resolved Reynolds stressSpalart (2009). A lot more empirical functions are implemented, some involves cell Reynolds number. Though they improved the accuracy of the model, those modifications make IDDES a rather complex model.

CHAPTER 3. DYNAMIC COMPUTING OF DDES MODELCONSTANT

3.1 The $\ell^2\omega$ DDES Model

As mentioned in section 2.3, DDES models which are based on modifying length scales in the dissipation term to reduce eddy viscosity make it unclear what the relation between DES eddy viscosity and LES subgrid viscosity is. For the eddy simulation branch of a DES model, in order to mimic a LES model, it would be preferable to make the eddy viscosity defined similar to LES formulation.

Our group has put forth an alternate formulation of DDES based on the $k-\omega$ RANS model [Reddy et al. (2014)]. It defines ν_T as an explicit function of ℓ_{DDES} 3.4. The production term in k equation contains ν_T. The other terms in the k and ω equations are unaltered. So the length scale limiter can be interpreted as limiting the production term, rather than enhancing the dissipation term. This alternate formulation of eddy viscosity is in similar form of Smagorinsky subgrid viscosity. Thus, a *priori* estimate of model constant $C_{DES} = 0.12$ was made from the Smagorinsky constant C_s. Then it is calibrated by channel flow simulations, a range of value $0.05 \lesssim C_{DES} \lesssim 0.15$ was found to be satisfactory.

The DDES formulation of Reddy et al. (2014) is reproduced here for convenience:

$$\ell_{DDES} = \ell_{RANS} - f_d \max(0, \ell_{RANS} - \ell_{LES}) \tag{3.1}$$

$$\ell_{RANS} = \frac{\sqrt{k}}{\omega} \tag{3.2}$$

$$\ell_{LES} = C_{DES}\Delta \tag{3.3}$$

$$\Delta = f_d V^{1/3} + (1 - f_d) h_{max} \qquad C_{DES} = 0.12$$

$$\nu_T = \ell^2_{DDES}\omega$$

The generic shielding function by Spalart et al. (2006) is also used here to provide shielding for the RANS branch. Using cubic root of cell volume allows the model to alleviate log-lay-mismatch, so the IDDES formulation is not required here. Test cases in Reddy et al. (2014) show that the DDES model with constant C_{DES} produces quite good results on different flows like channel flow, backward-facing step and periodic hills. Since one of the motivations to develop such model is to make the eddy simulation branch more like a practical LES model. It is natural that development of the Smagorinsky model shall be combined with current DDES model.

$$\frac{Dk}{Dt} = 2\nu_T |S|^2 - C_\mu k\omega + \frac{\partial}{\partial_j}[(\nu + \sigma_k(k/\omega))\frac{\partial k}{\partial x_i}] \tag{3.4}$$

$$\frac{D\omega}{Dt} = 2C_{\omega 1} |S|^2 - C_{\omega 2}\omega^2 + \frac{\partial}{\partial_j}[(\nu + \sigma_\omega(k/\omega))\frac{\partial \omega}{\partial x_i}] \tag{3.5}$$

It is known that the best value of Smagorinsky constant C_s depends on the flow configurations. For homogeneous isotropic turbulent the best value might be $C_s \approx 0.17$. For channel flow $C_s \approx 0.1$ is better than $C_s \approx 0.2$. For free shear flow $C_s \approx 0$. This could also be the case for the DDES model because the eddy viscosity formulation is similar to Smagorinsky type. Near wall the Smagorinsky model is too dissipative where a dynamic procedure or a damping function is required to decrease model constant. And in DDES model the near wall region is handled by RANS. RANS region thickness is an implicit function of C_{DES}. Optimized switching location requires carefully determined model constant C_{DES}. The dynamic process of determination of C_{DES} will be introduced in 3.2.

3.2 Dynamic Procedure for $\ell^2\omega$ DDES Model

The dynamic procedure used in current DDES model is similar to Lilly (1992). It is based on the germano identity. A set of assumptions are made to derive the evaluation process, as will be mentioned later.

In an LES simulation, the smallest stresses are being modeled. According to Kormogonov's hypotheses, those small scales are universal and not influenced by flow configurations. As shown in figure 3.1, turbulent motions in scales smaller than the grid scale Δ are being modeled and

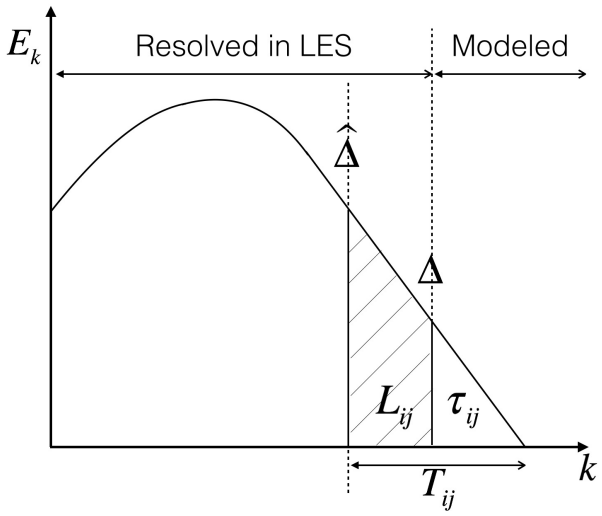

Figure 3.1: Rationale for dynamic procedureLilly (1992)

motions larger than that can be computed in LES. Resolved velocity is represented by $\bar{u}$ where the overbar means the LES filter. Note that in eddy viscosity models the LES filter is implicit. The unknown part is modeled by subgrid stress τ_{ij}. If we apply a test filter, which has a width of $\hat{\Delta}$ on that resolved field, it is equivalent to resolving the flow field on a coarser mesh. Then the subgrid stress is T_{ij}. Note that on the coarser mesh T_{ij} is unknown just like τ_{ij}. However, scales between test filter width $\hat{\Delta}$ and grid width Δ can be computed from resolved fields. The derivation of L_{ij}, the trace-free part of $T_{ij} - \hat{\tau}_{ij}$, is as follows,

$$\tau_{ij} = \bar{u}_i\bar{u}_j - \overline{u_iu_j} \tag{3.6}$$

$$T_{ij} = \hat{\bar{u}}_i\hat{\bar{u}}_j - \widehat{\overline{u_iu_j}} \tag{3.7}$$

$$dev(L_{ij}) = dev(T_{ij} - \hat{\tau_{ij}}) = dev(-\widehat{\bar{u}_i\bar{u}_j} + \hat{\bar{u}}_i\hat{\bar{u}}_j) \tag{3.8}$$

$dev()$ here means the deviatoric part. In a modeling sense, if we want to model the subgrid stress, the trace-free part can be represented by

$$\hat{\tau}_{ij} - \frac{1}{3}\hat{\tau}_{kk} = -2(C_{DES}\Delta)^2\widehat{\bar{\omega}\bar{S}_{ij}} \tag{3.9}$$

$$T_{ij} - \frac{1}{3}T_{kk} = -2(C_{DES}\hat{\Delta})^2\hat{\bar{\omega}}\hat{\bar{S}}_{ij} \tag{3.10}$$

Equation 3.9 is under the assumption that C_{DES} is unaffected by test filtering. The lenth scale in equation 3.10 is the test filter width. ω and S_{ij} need to be test filtered to represent the test filter scale value. Assume C_{DES} is scale independent, then we could define M_{ij} as equation 3.11, as a result equation represents the relation between L_{ij} and M_{ij}. Least square minimization is used to compute C_{DES} in form of equation 3.13.

$$M_{ij} = (\hat{\Delta}^2|\hat{\bar{\omega}}|\hat{\bar{S}}_{ij} - \Delta^2\widehat{|\bar{\omega}|\bar{S}_{ij}}) \tag{3.11}$$

$$L_{ij} \sim 2C_{DES}^2 M_{ij} \tag{3.12}$$

$$C_{DES}^2 = 0.5\frac{L_{ij}M_{ij}}{M_{ij}M_{ij}} \tag{3.13}$$

In current work, local averageing of $L_{ij}M_{ij}$ and $M_{ij}M_{ij}$ are used to help stabilizing the evaluated constant C_{DES}^2.

3.3 Constrains on Model Constant C_{DES}

Indeed, there is yet another issue, associated with the mesh resolution. In order for the test filter to be valid, a significant portion of the inertial range needs to be resolved. But the coarse meshes that sometimes are used in DES do not capture enough of the small scales. Figure 3.2(a) highlights this, where the power spectral density (PSD) of the streamwise velocity component u obtained in the simulation of a backward facing step is shown. The coarse mesh used results in a rather limited inertial range. A sketch of how the dynamic procedure works on coarse mesh is shown in Figure 3.2(b), the assumption made in equation 3.13 is that C_{DES} is scale independence which is not the case here. Applying dynamic procedure on those mesh could lead to underestimated C_{DES} value.

Figure 3.3(a) shows that f_d value is affected by C_{DES}. It is because C_{DES} defines LES length scale which determines eddy viscosity in eddy simulation region. f_d is based on wall

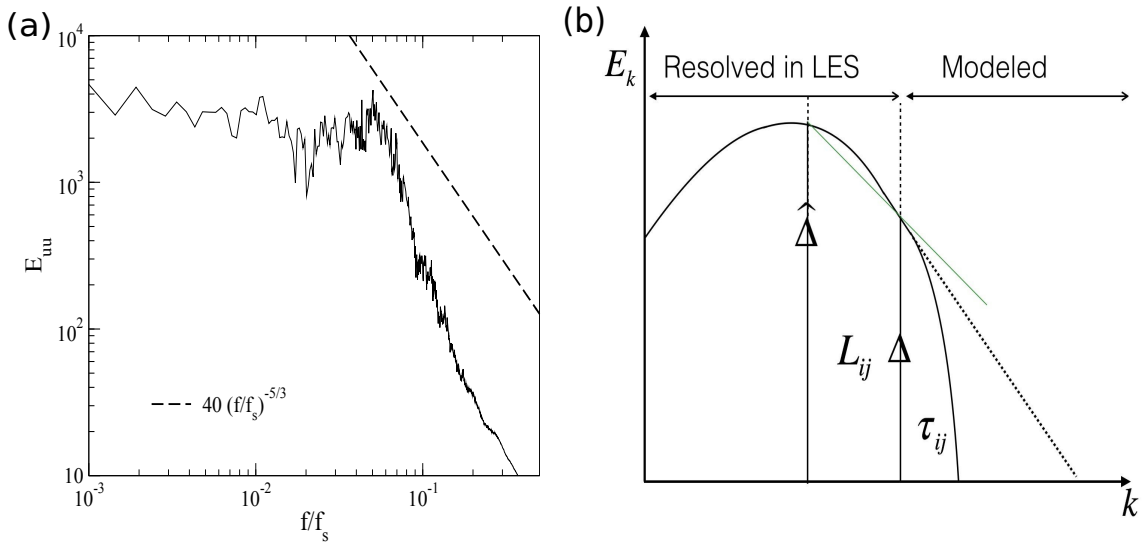

Figure 3.2: (a)PSD of stream velocity from backstep case. (b) Sketch of energy pectrum on coarse mesh

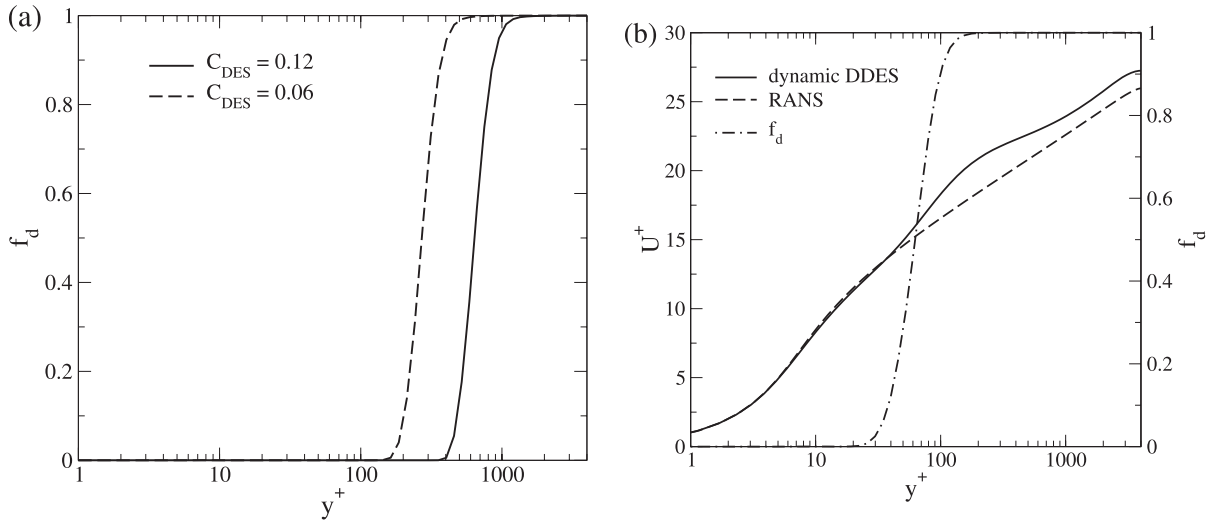

Figure 3.3: (a) f_d in channel flow with constant C_{DES}. (b) f_d and LLM on coarse mesh

distance and eddy viscosity. Reduction of C_{DES} value will reduce the eddy viscosity on top of the RANS/LES interface. As a result shielded region is lowered to further increase the eddy simulation region. This is why shielded RANS region is decreased due to underestimated C_{DES}, which acts like disabling the shielding process.

One thing needs to be noted that it is not all bad that C_{DES} is reduced by the dynamic procedure. In some case, enough inertial range is resolved. And even though a small C_{DES} value is computed in the dynamic procedure it is the appropriate value and is the case we want to improve the result. The case that deteriorates the result is only when there is not enough inertial range to determine C_{DES}, and it is underestimated. As a result, on coarse mesh that doesn't have enough inertial range resolved, avoiding the dynamic procedure altogether might be best. For anything but these very coarse meshes there is a good prospect for dynamic DES. Indeed, if the mesh resolution is close to that of wall resolved LES, utilizing the dynamic procedure might be favorable, even in the near-wall region. To address these caveats, we should introduce some evaluation criteria for mesh resolution.

In section 2.1.1, Kolmogorov's first similarity hypothesis defines the smallest scales of turbulent motions. We can use the ratio between grid spacing and some length scale similar to the Kolmogorov scale to define grid resolution. So we also define a length scale L_k which is in the same form as the kolmogorov scale. The dissipation is evaluated in equation 3.18, which contains both subgrid dissipation and modeled dissipation. One thing we need to note that we don't want to apply the dynamic procedure in the RANS region. So a modeled part comes into ϵ formulation to detect the RANS region.

$$C_{DES} = \max(C_{lim}, C_{dyn}) \tag{3.14}$$

$$C_{dyn}^2 = \max\left(0, \frac{L_{ij}M_{ij}}{2M_{ij}M_{ij}}\right) \tag{3.15}$$

$$C_{lim} = C_{DES}^0\left[1 - \tanh\left(\alpha \exp\left(\frac{-\beta h_{max}}{L_k}\right)\right)\right] \tag{3.16}$$

$$L_k = \left(\frac{\nu^3}{\epsilon}\right)^{1/4} \qquad h_{max} = max(\Delta X, \Delta Y, \Delta Z) \tag{3.17}$$

$$\epsilon = 2(C_{DES}^0 h_{max})^2 \omega |S|^2 + C_\mu k\omega \tag{3.18}$$

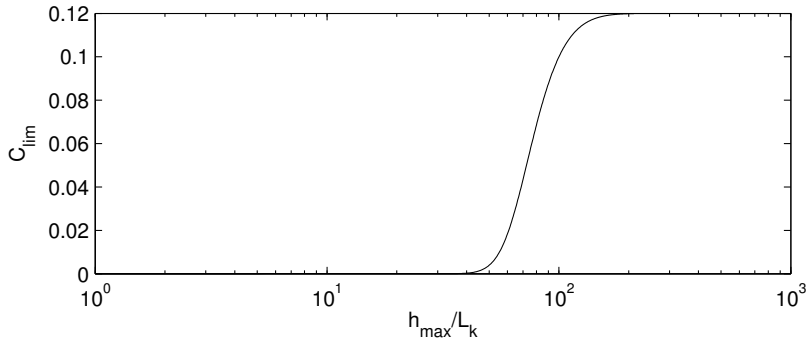

Figure 3.4: C_{lim} verses h_{max}/L_k

The grid spacing h_{max} is defined by maximum local cell spacing. If h_{max}/L_k is under a certain threshold value, it means the grid resolution is fine enough to apply the dynamic procedure. If h_{max}/L_k is approaching infinity, obviously the mesh is not capable of resolving enough portion of inertial subrange. Which means we should avoid using dynamic procedure. Here we introduce a limiting function which acts as a bound on the computed value of C_{DES}. It is described as follows:

h_{max} is the maximum cell spacing. Constants are defined as $\alpha = 25$ and $\beta = 0.05$. Those are empirical constants calibrated in channel flow test cases. It is a trade off between avoiding log-layer mismatch and maximizing area to apply dynamic procedure. Equation 3.15 is the same as equation 3.13, except that it is now clipped at 0, avoiding negative values for C_{dyn}^2. The limiting value as a function of h_{max}/L_k is plotted in figure 3.4.

CHAPTER 4. SIMULATION OF TEST CASES

The model is implemented into the open source CFD software OpenFOAM [Jasak et al. (2013)]. Gaussian finite volume integration with central differencing for interpolation was chosen for spatial discretization of equations. Convection terms of k and ω are limited by sweby limiter. Time integration was by the 2nd order, implicit backward difference method. The resulting matrix system was solved using the Pre-conditioned Bi-conjugate gradient algorithm, with the simplified, diagonal-based, incomplete-LU (Lower Upper) preconditioner. Solution for the matrix system at each time step was obtained by solving iteratively, to a specified tolerance of the residual norm. Maximum CFL number is controlled to be no larger than 0.5. For convenience, $\ell^2\omega$ DDES model with $C_{DES} = 0.12$ is termed as model 1 in test cases. The one with dynamic procedure is termed as model 2.

4.1 Test Cases for Dynamic Procedure

4.1.1 Channel Flow

Several channel flow simulations were carried out for different Reynolds numbers. The non-dimensioned velocity profiles are compared to the Dynamic Smagorinsky model or the $k-\omega$ model based on mesh resolution.

For figure 4.1(a), because the mesh resolution is fine, the RANS region is reduced to near wall region where ω is approaching infinity and is no longer proportional to $|S|$. The entire log layer is simulated by the LES branch of the DDES model. The non-dimensionalized velocity profile collapse with the one from dynamic smaoginsky model. For figure 4.1(b, c), in coarser mesh, non-limited region of C_{DES} gets reduced. Increasing of limiting value starts from the wall and then spread toward the channel center. For figure 4.1(d), in all the region within the

channel C_{DES} is limited to non-zero value which means the dynamic procedure doesn't apply in this case. In the eddy simulation of $Re_\tau = 6000$ case, the limiting value is $0.06 < C_{lim} < 0.12$. If the mesh is even coarse, then the limiting value shall increase to 0.12, which makes the model the same as model 1.

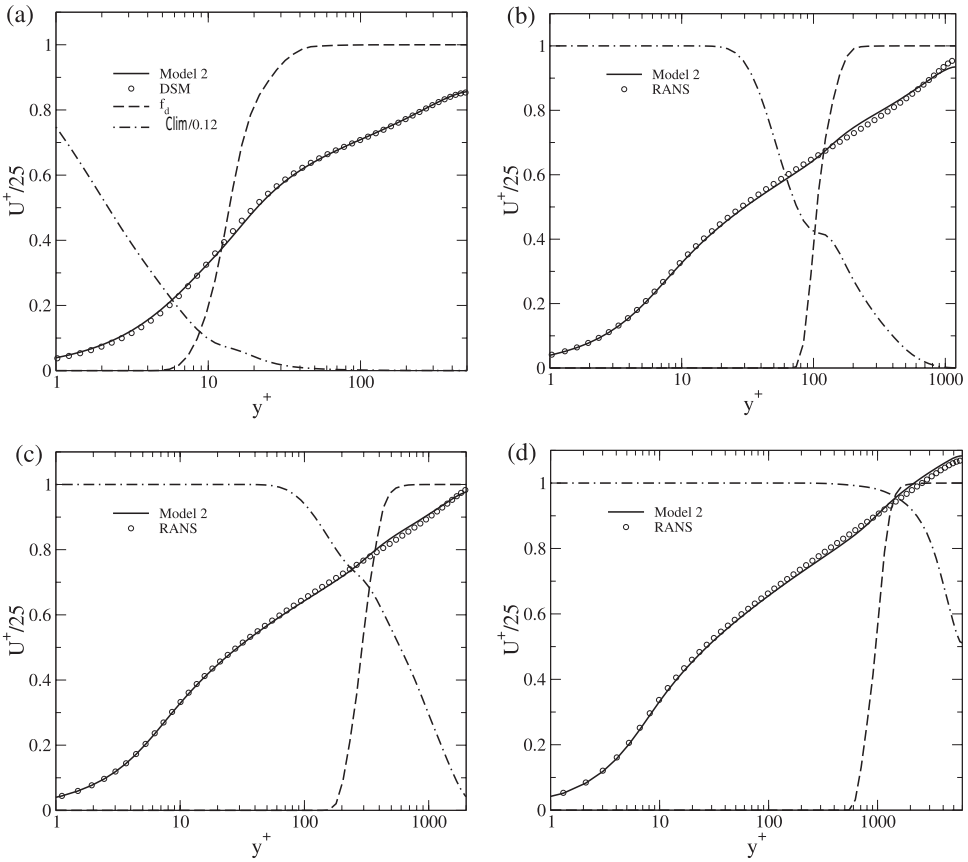

Figure 4.1: U^+ verses y^+ for channel flow with Re_τ=500, 1250, 2000, 6000

Re_τ	Δx^+	Δz^+
500	50	25
1200	120	60
2000	200	100
6000	600	300

Table 4.1: Grid resolution for channel flow cases with different Reynolds numbers

The difference between the performance of Model 2 and Model 1 is highlighted in figure 4.2. Model 1 and Model 2 data correspond to a channel flow simulation with $Re_\tau = 500$, while the

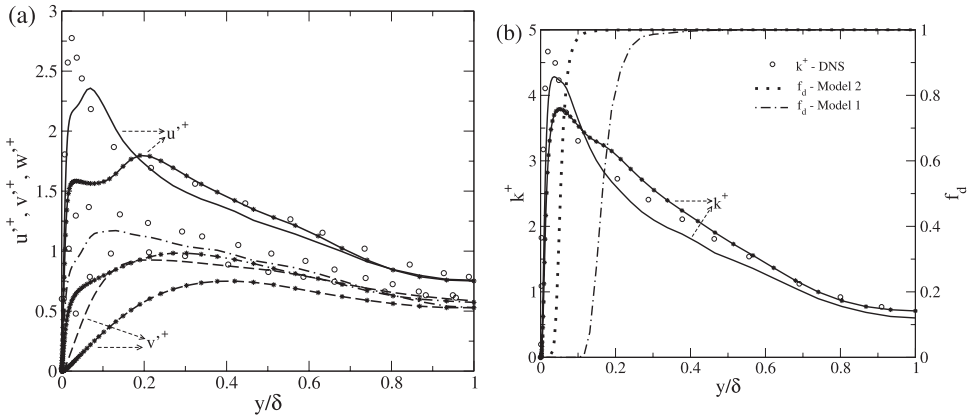

Figure 4.2: (a) Profile of Resolved u'^{+}, v'^{+}, w'^{+}, (b) Profile of k^{+} and f_d

DNS data correspond to $Re_\tau = 590$ [Moser et al. (1999)]. Profiles of resolved u'^{+} , v'^{+} , and w'^{+} are shown in Figure 5(a). The trend observed in the Model 1 predictions for this $Re_\tau = 500$ case is similar to that observed for $Re_\tau = 2250$ [Reddy et al. (2014)]. This is primarily due to the presence of a significant RANS region for Model 1 as shown in Figure 4.2(b), where the shielding function f_d is shown, along with the non-dimensional total turbulent kinetic energy k^{+}.

$$k^{+} = (k_m + k_r)/u_\tau^2 \tag{4.1}$$

$$k_r = 0.5(u'^2 + v'^2 + w'^2) \tag{4.2}$$

k^{+} here represent the total turbulent kinetic energy which is the sum of modeled part (k_m) and resolved part (k_r). Modeled part is the k value got from k equation. Resolved part is defined in equation 4.2.

Notice that the extent of the RANS region is similar for Model 1 with $Re_\tau = 500$ and $Re_\tau = 2250$, despite the fine mesh for the lower Re_τ . Model 2 however was able to detect that the mesh has sufficient resolution to employ the dynamic procedure. This leads to lower C_{DES} , and subsequently, lower k and ℓ_{LES} values, resulting in a smaller shielded region. Thus, the eddy simulation branch is active over a larger region, till the bottom of log-layer by maximum, which gives a better prediction of the velocity fluctuations and the turbulent kinetic energy.

4.1.2 Backward-facing Step

The flow over a backward facing step is an excellent case to test the performance of any hybrid RANS/LES method due to the abrupt change in flow features across the sharp edge. The model must be capable of switching from RANS to eddy simulation at the step, where the flow separates.

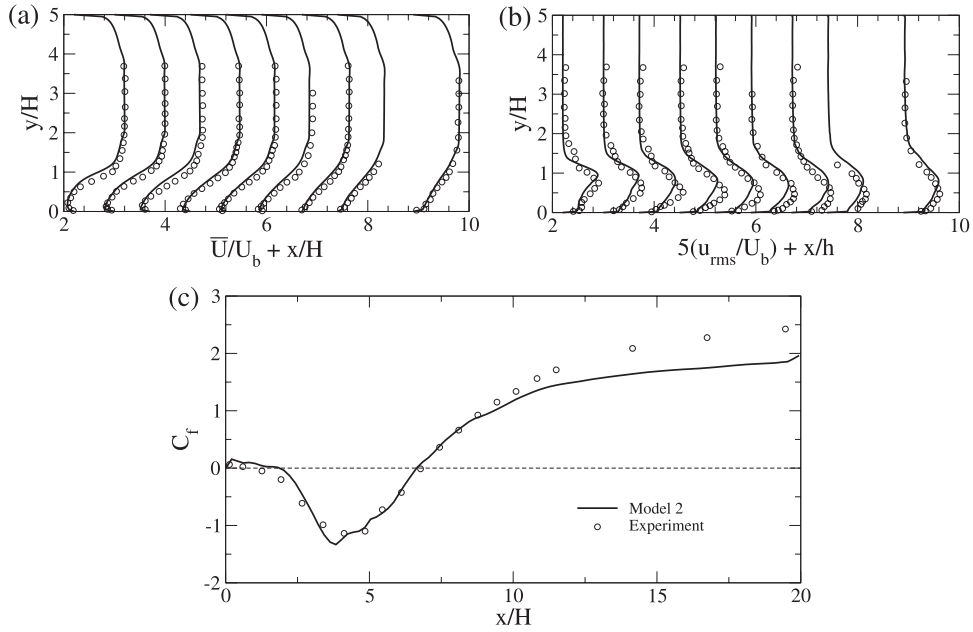

Figure 4.3: (a) Mean velocity distribution at different streamwise location. (b) Mean u_{rms} profile at different streamwise location. (c) C_f distribution along bottom of channel

The experimental setup of Vogel and Eaton (1985) was simulated. The Reynolds number at the inflow boundary is $28,000$ based on the bulk velocity U_b and the step height H. Simulation details such as the grid used, the boundary conditions specified and the extent of the computational domain are the same as in Reddy et al. (2014).

Overall, a good agreement between the simulation and the experimental data is observed. Figures 4.3 shows velocity profile after step, u_{rms} profile after step, and the variation of the skin friction coefficient C_f along the bottom wall and it agrees experimental data quite well.

The grid used is relatively coarse ($\Delta x^+ \approx 200$ and $\Delta z^+ \approx 100$ away from the step), so we expect the limiting function to impose lower bounds on C_{DES}. Figure 4.4 shows contours of time-averaged C_{lim}. We observe that almost throughout the entire eddying region, $C_{lim} > 0.06$.

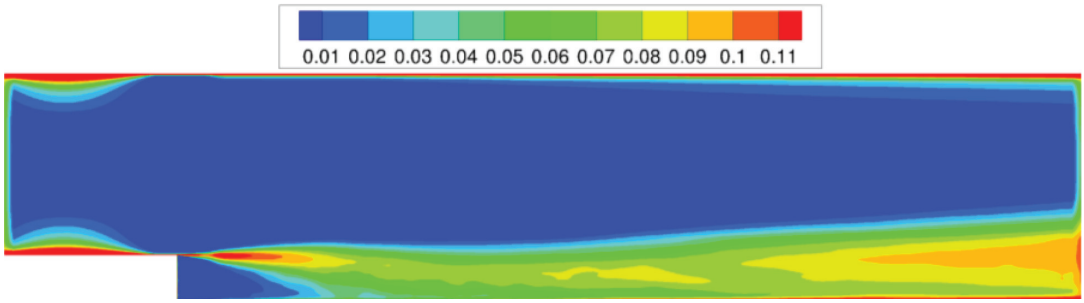

Figure 4.4: Time averaged C_{lim} along central plane

C_{DES} hits the limiter at 0.12 where the flow separates from the step. Due to wall resolution requirements, the cell at the separation corner has very large aspect ratio, which deviates from typical LES grid resolution. Also, the rate of strain is large, which means that dissipation is high. As a result, the values of L_k are relatively low, causing the bound on the value of C_{DES} to be invoked.

4.1.3 Periodic Hills

This case shows flow separation from a smooth surface, unlike the backward-facing step. The geometry and flow conditions are described in Fröhlich et al. (2005). The extent of the computational domain is $9H$ and $4.5H$ along the streamwise and spanwise directions respectively, where H is the hill height at the crest. The Reynolds number based on the hill height and the bulk velocity at the crest is $10,595$. The grid used has $106 \times 100 \times 90$ points in the streamwise, wall normal and spanwise directions respectively. Periodic boundary conditions are enforced along the streamwise and spanwise directions. The flow is driven by a pressure gradient source term which is adjusted to sustain the required bulk velocity at the inflow boundary.

Figure 4.5(a) compares skin friction coefficient along bottom wall predicted by Model 1 and Model 2 with LES data [Fröhlich et al. (2005)]. Overall there is a good agreement between those 2 models and LES data. Model 2 seems predict a better match, especially near the inlet. This maybe because grid is finer near the hill, and model 2 can reduce the RANS region thickness at that location. Figure 4.5(b, c) shows the velocity profile and u_{rms} profile agree with the LES data. Thanks to the periodic boundary condition, U_{rms} profile fits the LES data well at

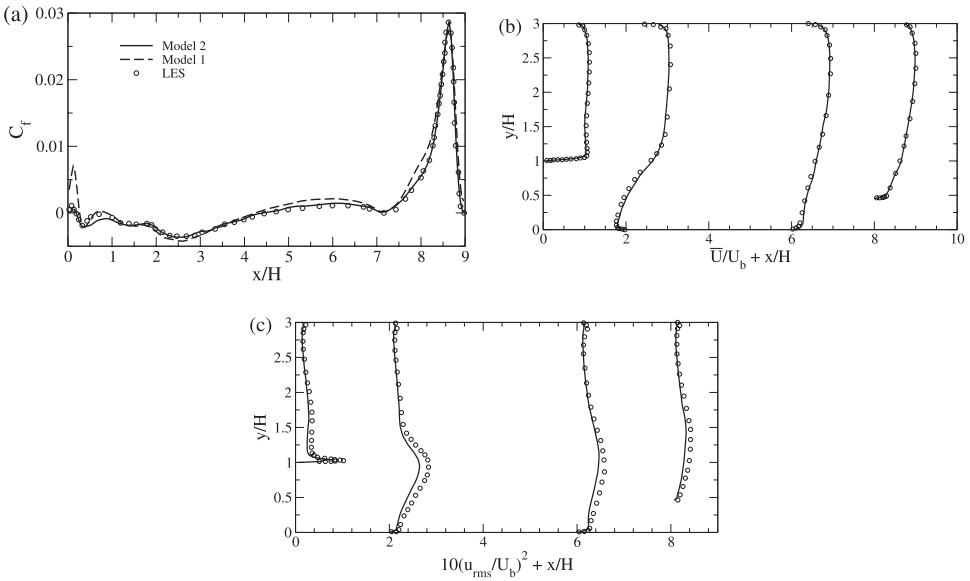

Figure 4.5: (a) C_f distribution along bottom wall. (b) Mean velocity profile at different streamwise location. (c) Mean u_{rms} profile at different streamwise location.

the top of the hill ($x/H = 0$), which is definitely helpful in such smooth surface separation situation.

4.1.4 Rotating Channel

The flow through a fully developed rotating turbulent channel was simulated as another illustration of the advantage of the dynamic procedure over a constant C_{DES}. In pure RANS mode, $k-\omega$ would require some kind of curvature correction to predict rotation effect [Arolla and Durbin (2013)]. No such corrections are used here. This means that simulations based on Model 1 would likely be subject to errors due to the presence of a thick RANS region near the walls. In the eddy-simulation region, rotation effects are captured by the Navier-Stokes equations. Thus, we expect to get better results using Model 2 since the RANS region will be smaller, provided the mesh is fine enough for LES simulation.

The non-dimensional measure of rotation is defined as the Rossby number $Ro = 2\Omega\delta/U_b$ [Grundestam et al. (2008)], where U_b is the bulk velocity, δ the channel half-width and Ω the rate of coordinate system rotation. Four different simulations were carried out, corresponding to four different Ro values. These simulations correspond to previous DNS studies of Grundestam

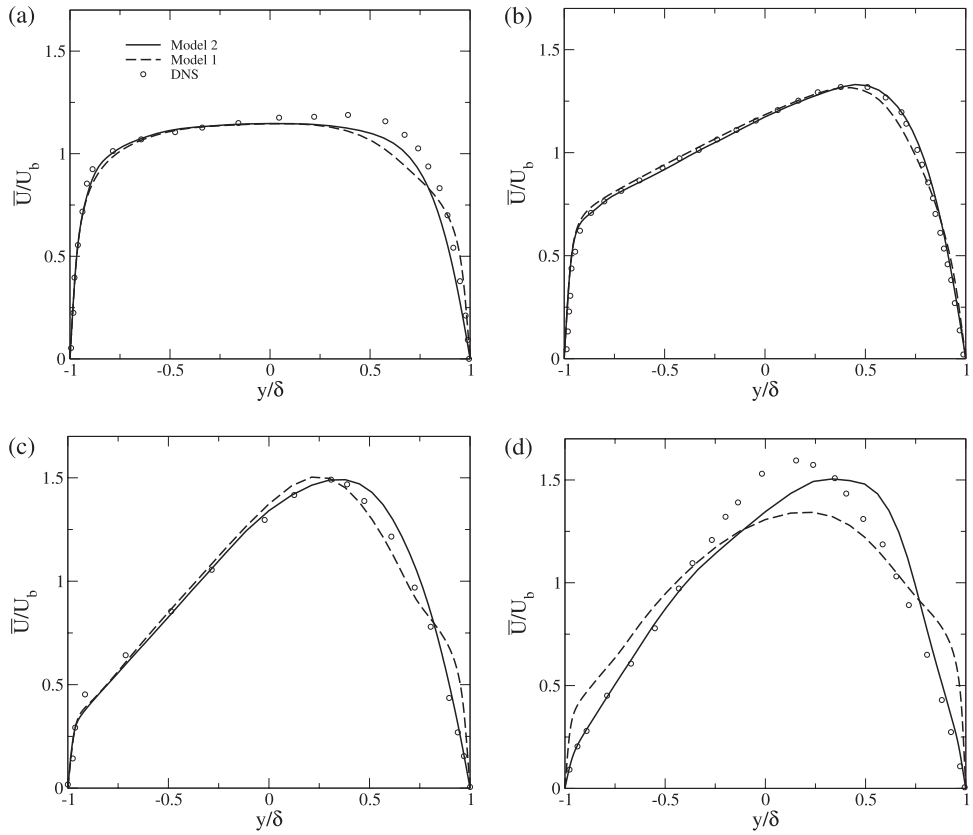

Figure 4.6: Mean velocity profile at (a) $Ro = 0.1$, (b) $Ro = 0.5$, (c) $Ro = 0.98$, (b) $Ro = 1.5$

Grundestam et al. (2008) ($Ro = 0.98, 1.5$) and Kristoffersen Kristoffersen and Andersson (1993) ($Ro = 0.1, 0.5$).

	Re_τ		
Ro	DNS	Model 1	Model 2
0.1	194	229	196
0.5	194	206	199
0.98	180	215	179
1.5	180	330	187

Table 4.2: Predicted Re_τ for different Ro values

In the DNS studies, a constant pressure gradient was prescribed, which forces constant total u_τ and Re_τ values. The bulk velocity, U_b and Re_b (Reynolds number based on the bulk velocity) then vary with Ro. In our simulations, U_b was specified, for each Ro, and the resulting

u_τ and Re_τ values were computed. Figure 4.6 shows mean velocity profiles obtained with both Model 1 and Model 2, compared with DNS data. Model 2 results are more in line with the data, especially near the right wall, at higher Ro, where the turbulence is suppressed by rotation. Due to the asymmetry in the velocity profile, there are 2 different friction velocities, $u_{\tau u}$ and $u_{\tau s}$, corresponding to the unstable and stable sides Grundestam et al. (2008). An average friction velocity u_τ is defined as:

$$u_\tau = [0.5(u_{\tau u}^2 + u_{\tau s}^2)]^{1/2}$$

For the specified bulk velocity U_b, the predicted Re_τ values for Model 1 and Model 2 are shown in table 4.2, along with the reference DNS values. Model 2 predicts more accurate values for the wall shear stress than Model 1. The grid used for these cases has a non-dimensional cell spacing $\Delta x^+ = \Delta z^+ \approx 30$ for Model 2 (the corresponding numbers evaluated when using Model 1 ≈ 50 due to the larger predicted u_τ), with $\Delta y^+ < 1$ for the near wall cells in all the simulations. This leads to a smaller RANS region while using Model 2, and subsequently a smaller error stemming from the absence of any curvature correction terms.

At large Ro, we observe that Model 2 starts to deviate from the DNS results, especially on the right wall (figure 4.6). That is the wall where rotation is stabilizing. A likely explanation for the discrepancy is that the RANS model does not include a curvature correction. Hence, as long as there is a thin RANS region, it cannot laminarize. Regions of negative production were observed for $Ro = 1.5$ Grundestam et al. (2008), and that certainly cannot be captured by the $k-\omega$ eddy viscosity model. For lower Ro values, the predictions are in good agreement with DNS.

Also, as Ro gets higher the flow starts to relaminarize. We should expect C_{DES} value to get closer to zero if our model is responding to flow. Figure 4.7 shows how C_{DES} and C_{lim} distribute inside channel. Near wall it is expected C_{DES} to be large because it is RANS region. In side the channel C_{DES} value is not symmetric. It is because on the top side on channel turbulence is enhanced and on the bottom side turbulence is depressed. Model constant values in figure 4.7 verifies that the dynmaic procedure can respond to these rotation effects.

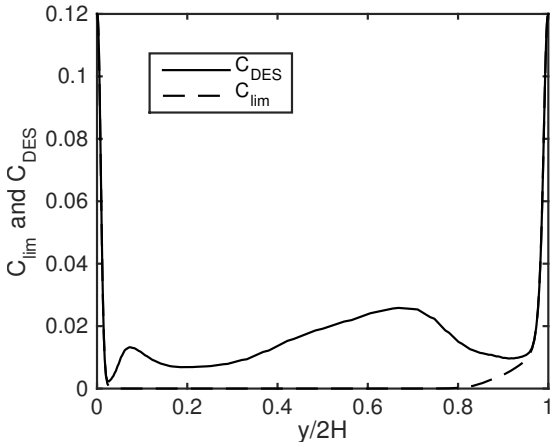

Figure 4.7: C_{DES} and C_{lim} value across channel at $Ro = 1.5$

4.1.5 3D Diffuser

As an example of a 3D geometry, the flow through a 3D diffuser was simulated. The geometry and flow conditions correspond to the "diffuser 1" of Cherry *et al.* Cherry et al. (2008). The grid and boundary conditions are the same as in Jeyapaul (2011). The grid is nearly LES-quality. Three simulations were carried out for this geometry, each corresponding to a different turbulence model – the $k-\omega$ RANS model Wilcox (1993), Model 1 Reddy et al. (2014) and Model 2 (the current dynamic DDES model).

Figure 4.8 shows contours of the time-averaged streamwise velocity component obtained from all three simulations at the diffuser exit ($x/H = 15$, where H is the height of the inlet section). Model 1 does predict separation along the top wall, but the separation region is much thinner than the DNS data. Figure 4.9 and figure 4.10 compared the mean velocity profiles at $x/H = 0$, 2, 6, 8, 12, 14, 15.5 and 17 along the midplane obtained for Model 1 and Model 2 with DNS data. It shows better prediction from Model 2 than Model 1.

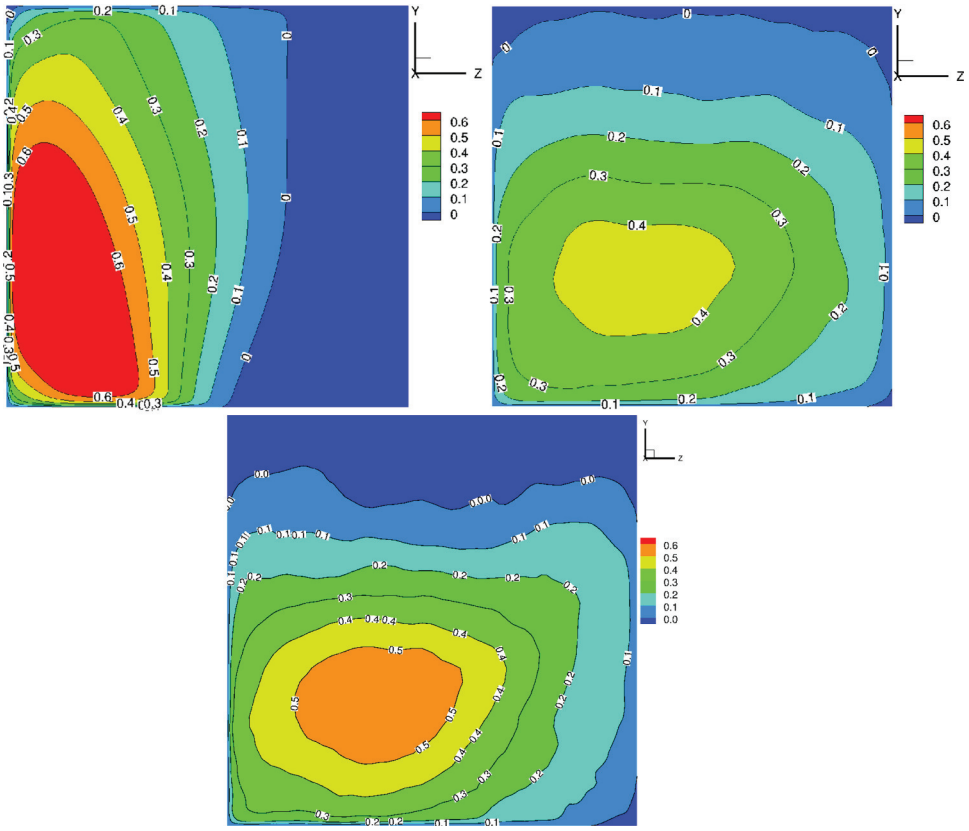

Figure 4.8: Mean streamwise velocity contour at diffuser exit

Introducing the dynamic procedure improves the results appreciably. The dynamic DDES was able to take advantage of the grid resolution. Utilizing the dynamic procedure almost everywhere in the domain, leading to marked improvement in the prediction.

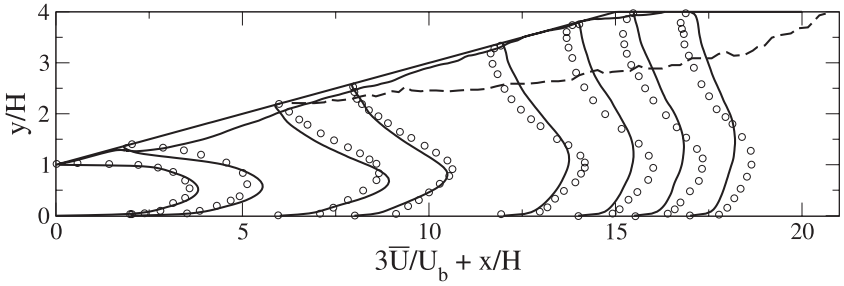

Figure 4.9: Mean velocity distribution along diffuser central plane with Model 1

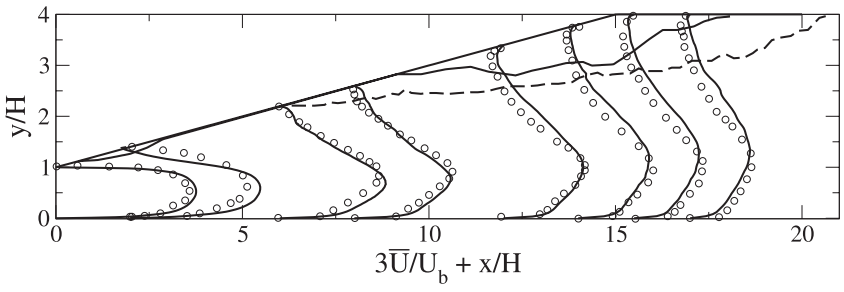

Figure 4.10: Mean velocity distribution along diffuser central plane with Model 2

4.1.6 FAITH Hill

FAITH hill [Bell et al. (2012)] is an axisymmetric hill defined by cosine curve. Those massive separation flow should be well handed by DES method. The computational domain is the same as in the experiment. The boundary layer start from a leading edge which has the same location relative to the hill as in the experiment. The Reynolds number based on hill hight is $500,000$, the separated regiona after the hill is large. So high Reynolds number and massive separation makes this flow configuration a perfect case for nature DES application. Uniform flow is imposed before the leading edge just like the experiment. Boundary layer grows under RANS branch. The mesh used has non-dimensional cell spacing ΔX^+ and ΔZ^+ up to 1000 bsed on local friction velocity.

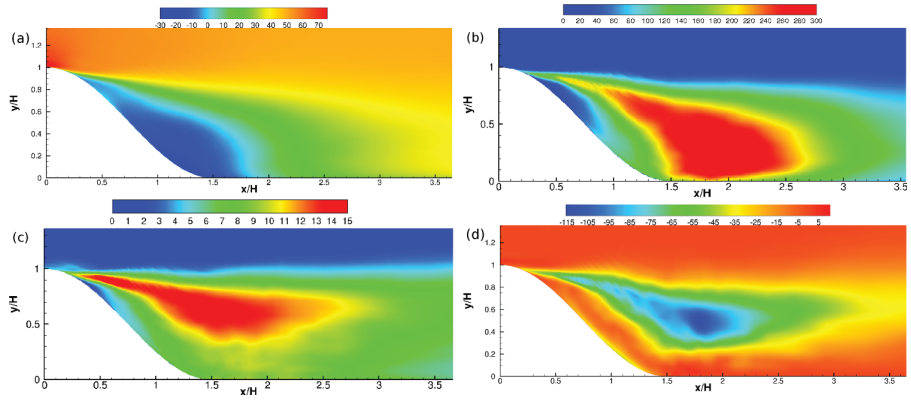

Figure 4.11: (a) Mean streamwise Velocity, (b) total TKE, (c) Mean u_{rms}, and (d) Mean u'v' on $Z = 0$ plane

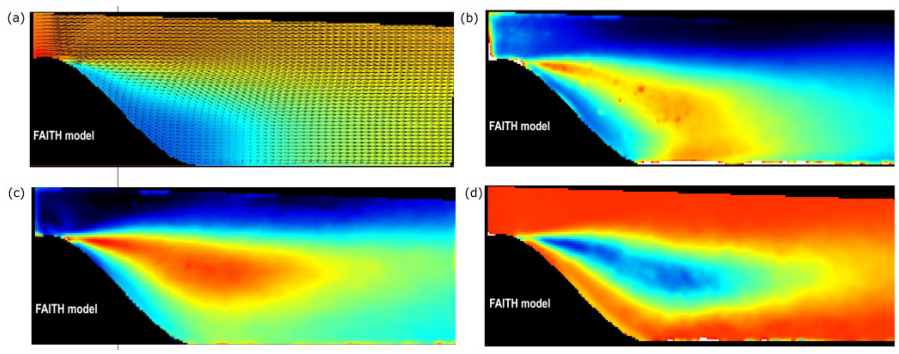

Figure 4.12: Contour of experimental data, (a) Mean streamwise Velocity, (b) TKE, (c) Mean u_{rms}, and (d) Mean u'v' on $Z = 0$ plane, figure taken from Bell et al. (2012). Color bands are the same as figure 4.11

Figure 4.11 shows time average streamwise velocity, total turbulent kinetic energy(TKE), u_{rms} and $u'v'$ on streamwise and wall normal plane across hill center. Figure 4.13 shows time averaged modeled and resolved parts of TKE, the shielding function f_d and time averaged value of C_{DES}.

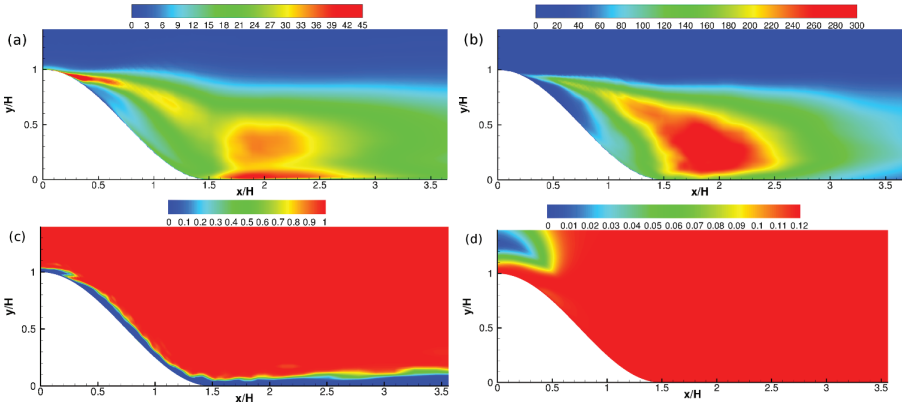

Figure 4.13: (a) Mean modeled TKE, (b) Mean resolved TKE, (c) f_d, and (d) Mean C_{DES} on $Z = 0$ plane

Several things need to be noted when comparing DES prediction (figure 4.11) and experimental data (figure4.12). The area of the separated region predicted by DES model matches experimental data. And the velocity profile matches well, as shown in figure 4.14. The trends observed in the u_{rms} and k variations in the PIV data are captured by the simulation. The

peak value is slightly overestimated for u_{rms}. k is obviously overpredicted. One possible explanation for this would be the coarseness of the mesh used. LES in coarse mesh usually will have overpredicted streamwise velocity predictions, do does the DES model show in this case. C_f distribution on hill predicted by Model 2 gives good agreement with experimental data, as shown in figure 4.15.

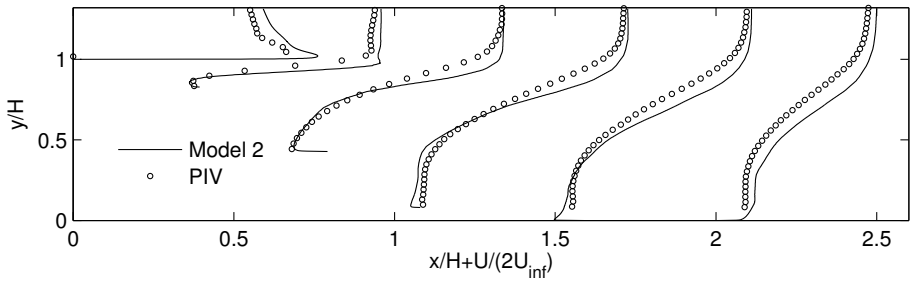

Figure 4.14: Velocity profile predict by Model 2 compared with experiment (Bell et al. (2012))

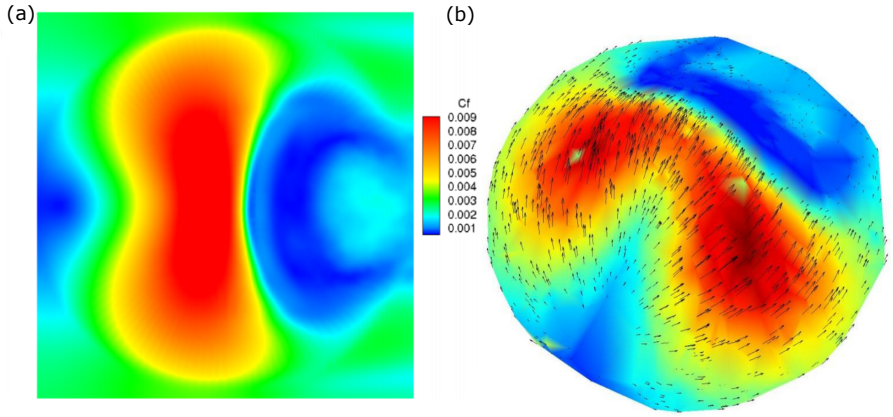

Figure 4.15: C_f predicted on hill by (a) Model 2, (b) Experiment by Bell et al. (2012)

The fact that the mesh is coarse can also be inferred from figure 4.13(d) which shows that $C_{DES} = C^0_{DES} = 0.12$ over the entire region behind the hill, where we observe most of the relevant unsteady phenomena. Comparison between the $u'v'$ distribution shows that with RANS inlet profile, after separation the resolved turbulnet content needs to develop over certain streamwise direction to reach a normal value. In this case, because C_{DES} is large, Model 2 essentially functions as Model 1 for simulations involving very coarse meshes. Better agreement

with experimental data could likely be achieved by increasing the mesh resolution such that the dynamic procedure is employed in the eddy simulation regions.

4.2 Exploring the Role of Inlet Conditions

DES was proposed to address massive separated flow. Flow with shallow separation or weak instability is considered as challenging for DES. There are still some unresolved issues in the RANS/LES interface. Usually DES will give poor results when those regions that determine flow features is located in this interface. In some cases, this can be alleviated by using turbulent inflow conditions to speed up the RANS to LES transition to improve the prediction accuracy.

For example, for backward-facing step 4.1.2, before the step flow is attached boundary layer but right after the step the model switches from RANS to LES branch. Right after the switch, there is the region that resolved turbulent stress needs to be developed. Before the total stress recovers, there is an unphysical region in RANS to LES transition area. The length of that area is dependent on the flow. However, flow instability after backward-facing step is strong and turbulent stress can recover to an appropriate magnitude soon enough that good agreement with experimental data is achieved.

4.2.1 NASA 2D Bump

There are flow control experiments on separation on this geometry [Seifert and Pack (2002)], however this is not the focus here. In this section we only simulate flow over NASA 2-D bump without flow control or corresponding slots and chamber. It is similar to the periodic hills because the flow separates from a smooth surface but the difference is that we can control the inlet condition in this case. Totally the mesh contains 0.8 million cells for RANS inlet case and 1.3 million cells for unsteady inlet. Extra cells are used for an extended domain. The non-dimensional mesh spacing is $100 < \Delta X^+ < 500$ and $100 < \Delta Z^+ < 200$ based on different locations in the domain. For inflow condition using RANS profile, a precursor simulation is performed to obtain a RANS boundary layer profile just the same as in [Avdis et al. (2009)] except their precursor simulation is using LES. The imposed inlet plane is the same as in Avdis et al. (2009). For inlet profile generated by rescaling and recycling [Arolla and Durbin

(2014)], the domain is extended to $x/C = -2.1$ which allows a recycling region allocated at $-2.1 < x/C < 1.38$ to generated certain boundary layer thickness to match the LES data.

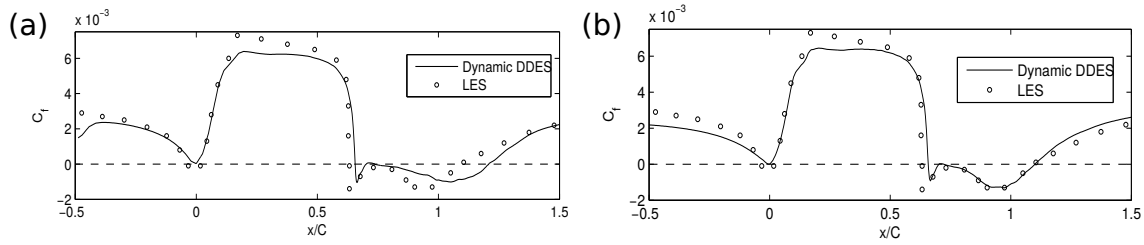

Figure 4.16: Cf distribution along bottom wall compared with LES Avdis et al. (2009), (a) with RANS inlet, (b) with unsteady inlet

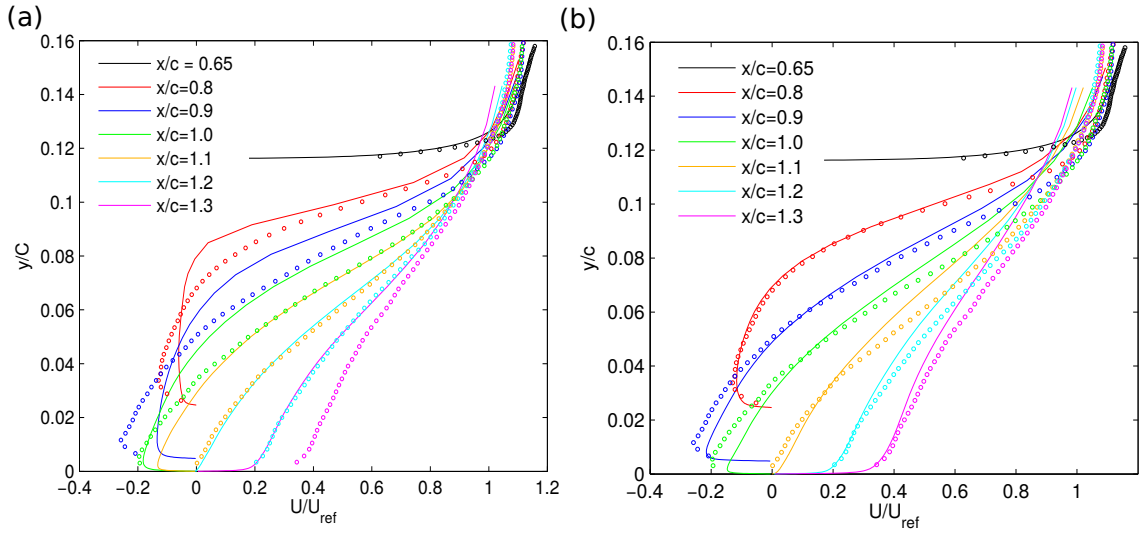

Figure 4.17: Velocity distribution after hump compared with LES Avdis et al. (2009),, (a) with RANS inlet, (b) with unsteady inlet

Figure 4.16 shows that if a RANS profile is used, which means before separation the attached boundary layer is handled by the RANS branch, the predicted reattachment location($x/C \approx 1.22$) is later than in LES. In another words, DES performance in such smooth surface separation condition is similar to RANS. It is consistent with other DES simulations [Avdis et al. (2009)]. Also this is approximately the reattachment location predicted by other RANS models [Avdis et al. (2009)]. The WMLES case, where velocity fluctuations are imposed at the inlet, predicts a reattachment location close to LES data. The velocity profiles after the hump

crest are also shown in figure 4.17. A good agreement with experimental data can be observed [Rumsey (2015)]. However, the natural DES case predicts an incorrect velocity profile right after separation. This is because in the natural DES case, right after separation modeled stress is reduced due to decreased eddy viscosity, the total stress is underpredicted. Although the model switches to its LES branch, there is not enough resolved turbulence because the flow is just convected out of the attached boundary layer which is a RANS region. In such separation from a smooth surface, the shear layer instability is not very strong, which means a certain streamwise length is required for resolved Reynolds stress to develop. This kind of mechanism is plotted in figure 4.18(a), resolved Reynolds stress is nearly zero at $x/C = 0.65$ and it grows slowly post hump. On the plot as the flow goes downstream, the resolved Reynolds stress becomes closer and closer to experimental data. However, for the WMLES case, in figure 4.18(b), resolved Reynolds stress is approximately at the same level as experimental data. The difference may lie in near wall region but it is somehow unavailable in experimental data. After the flow separates, the resolved part has a similar magnitude as the experimental data, though not perfect match. It is possibly because the mesh is coarse.

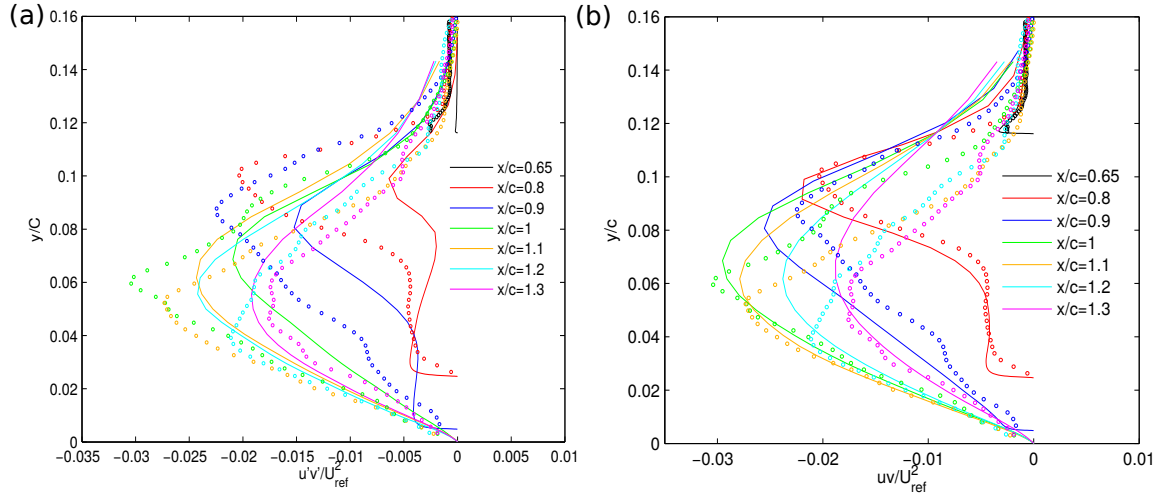

Figure 4.18: Reynolds stress u'v' distribution after Hump, (a) with RANS inlet, (b) with unsteady inlet

However, this is one of the cases that can tell the influence of using different inlet condition. For smooth surface separation or cases sensitive to the RANS/LES interface, turbulent fluctuations are needed in the inflow condition.

4.2.2 ERCOFTAC Hill

This is another axisymmetric hill which is lower than the FAITH hill. The geometry and flow configurations are described in Garcia-Villalba et al. (2009). The Reynolds number based on free stream velocity and hill hight is $130,000$. In the absence of the hill, a zero-pressure-gradient turbulent boundary layer thickness δ is half the hill height. The separated region is extremely shallow. Shallow separation cases are expected to be challenging for DES which is not naturally designed for this situation. There is an enormous discrepancy between results from RANS [Visbal et al. (2007)] and LES [Garcia-Villalba et al. (2009)]. The surface streamline topology predicted by RANS is totally different with LES and experiments.

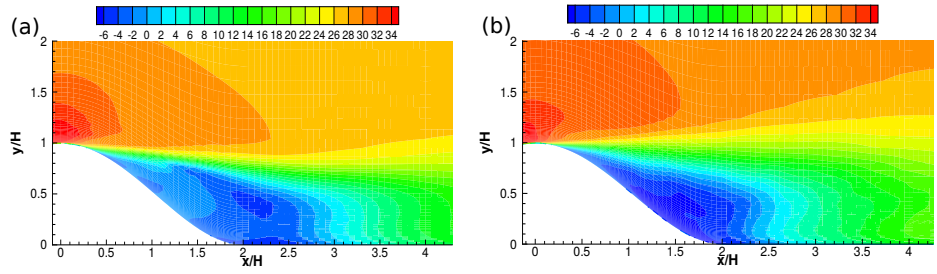

Figure 4.19: Mean streamwise velocity contour, (a) with RANS inlet, (b) with unsteady inlet

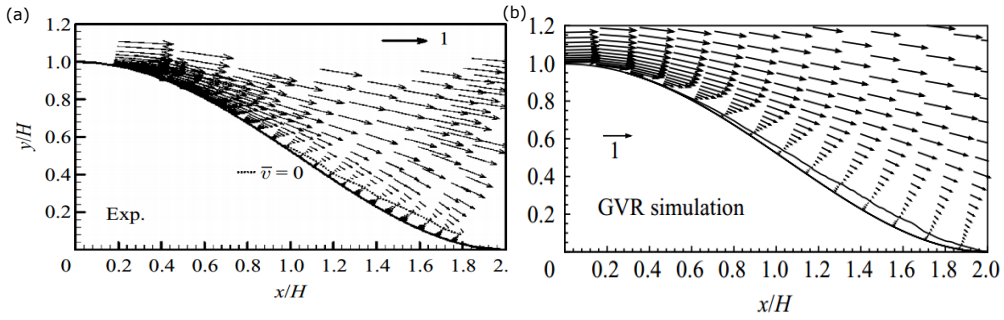

Figure 4.20: Central plane velocity vector and separation line, (a) Experiments, (b) LES. Figures taken from Garcia-Villalba et al. (2009)

Since this is a case with shallow separated region, the inflow condition can actually make some difference in the result. Two simulations are performed here. The first is using inlet profile prescribed by $k-\omega$ RANS. The second is using recycling and rescaling of upstream boundary layer [Arolla and Durbin (2014)]. Totally there are approximately 3 million cells in the domain. This simulation was carried out before the dynamic model was developed, so a constant $C_{DES} = 0.06$ was used in the simulation.

The result from the simulation shows that there is no obvious improvement compared to RANS models. In DDES, the near wall region is covered by RANS. In experiments and LES simulations the separated region is very shallow [Garcia-Villalba et al. (2009)]. If we assume that the DES model can predict a corrected separation region. Then the separation region is so shallow that almost all of it is covered by RANS. So as a result this is a case that the near wall RANS region plays a dominant role. Unfortunately the RANS model, predicts wrong surface streamline topology and separation bubble. The DES model only gives better turbulent statistics by resolving turbulent motions in the eddy simulation region. It is hard to imagine how much improvement can the RANS region get from eddy simulation region. In this case, we do observe such behavior. In figure 4.25, DES with RANS inlet profiles predicts earliest separation location compared to the case with inlet fluctuations. The dominant role of the RANS model in such case limits the extent to which DES can improve the predictions. The reattachment location and separation bubble are similar to the RANS results [Visbal et al. (2007)] even for the WMLES case.

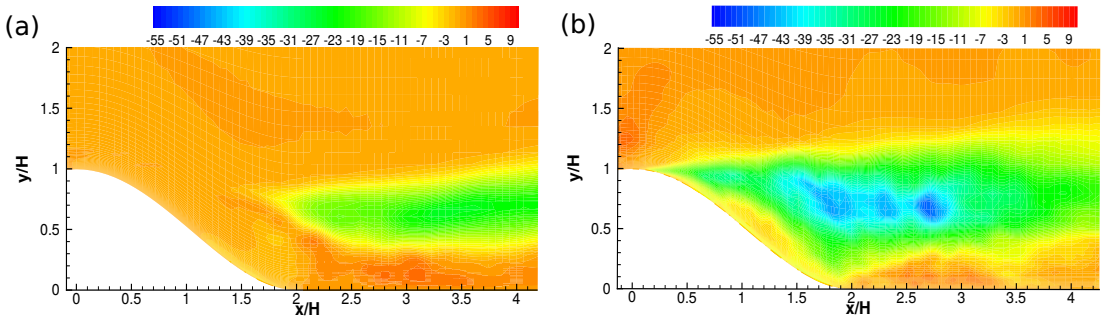

Figure 4.21: Mean resolved Reynolds stress u'v', (a) with RANS inlet, (b) with unsteady inlet

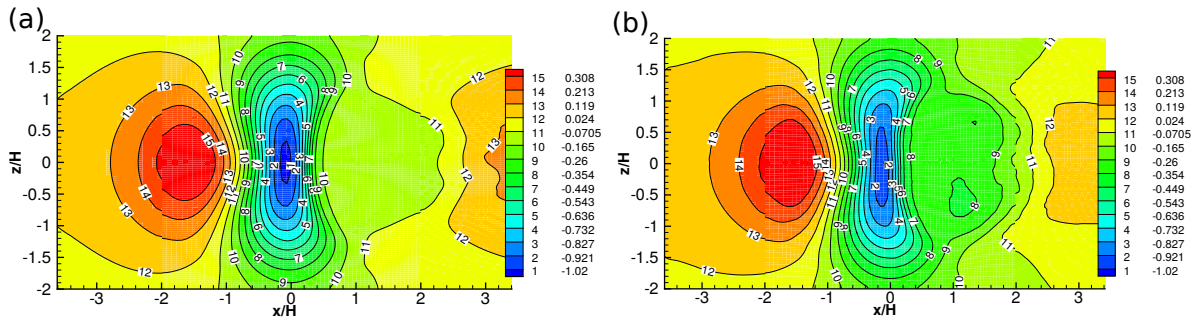

Figure 4.22: Cp contour On hill surface, (a) with RANS inlet, (b) with unsteady inlet

However, this geometry is also a challenging case for LES. The fine mesh LES case (GVR) [Garcia-Villalba et al. (2009)] has approximately 135 million cells which is about to be nearly fifty times finer than our case. It also predicts earlier separation location than experiment and the Cp curve doesn't fit experimental exactly. One thing we can get from the result is that for those cases with shallow separation, inlet condition does make a big difference in the results.

Figure 4.21 shows resolved Reynolds stress u'v' after the hill. In the nature DES case, it takes a long distance for it to grow. The real reattachment location is so close to the hill that it cannot wait for Reynolds stress to be developed that slow. For the WMLES application, though the resolved Reynolds stress develops much faster than nature DES application, it is only capable of suppressing the separation bubble to a level similar to RANS. In figure 4.21, the near wall region doesn't have enough resolved Reynolds stress clearly shows that. The surface streamline plot shows a topology more similar to RANS [Visbal et al. (2007)] rather than LES results [Garcia-Villalba et al. (2009)]. In DES predicitions saddle points (red cube) near separation line are missing and are possibly merged with separation point (blue dot in figure 4.24(b)). The other two saddle points (red cube) near reattachment location are missing, too. Most likely those two are merged with the reattachment point, which is also marked in blue in figure 4.24(b). In figure 4.24(a) on hill surface large k value is observed but this can not be captured by the $k-\omega$ RANS model. This maybe is related to the failure of DES model in this case because RANS is used to handle near wall region.

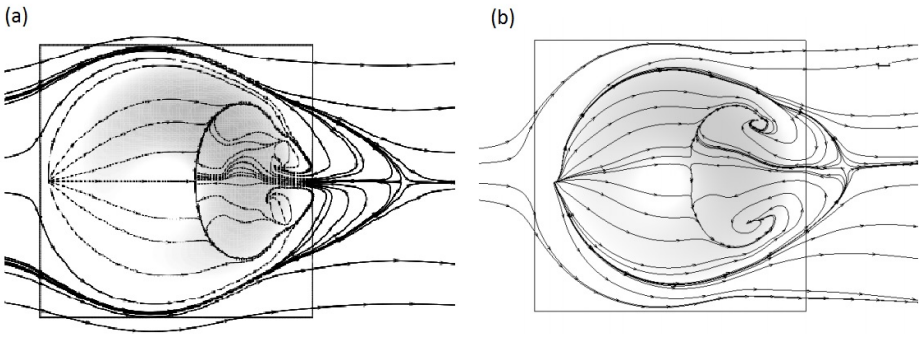

Figure 4.23: Surface streamline, (a) with RANS inlet, (b) with unsteady inlet

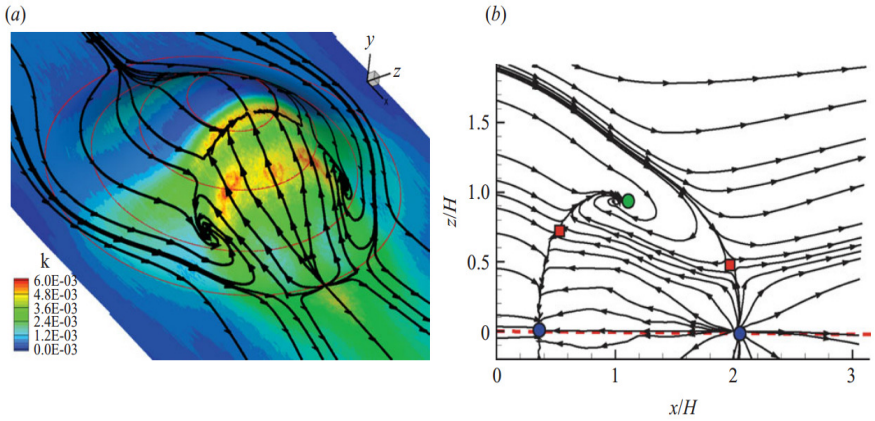

Figure 4.24: LES data from GVR [Garcia-Villalba et al. (2009)], (a) Surface streamline on hill, (b) Surface streamline topology. Figures taken from Garcia-Villalba et al. (2009)

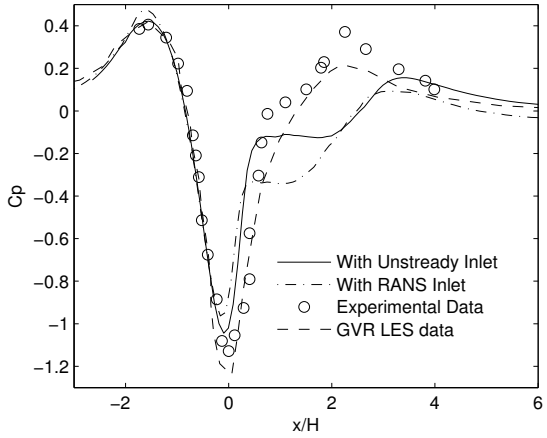

Figure 4.25: Pressure coefficient on hill at Z=0

CHAPTER 5. CONCLUSION

The previously proposed, DDES formulation of Reddy et al. (2014) opened the possibility to develop a dynamic DDES formulation. The model constant C_{DES} is computed locally via a well-established procedure. This requires a test filter that captures the small scales. Coarse grids are sometimes used for DES, and these small scales are not present. A limiting function was introduced in order to estimate the validity of utilizing the dynamic procedure on the given mesh. The function compares grid spacing to a Kolmogorov scale. Based on this, C_{DES} becomes a default value if the dynamic procedure is likely to fail. Simulations showed improved predictions when employing the dynamic procedure, rather than using a constant C_{DES}. That was especially true when simulations were carried out on LES-quality meshes.

The dynamic procedure yields superior performance over the constant coefficient model for 2 reasons. The first reason is similar to the case of LES: the coefficient adapts to how well the turbulence is resolved; if it is well resolved C_{DES} becomes very small. The second reason is peculiar to detached eddy simulation: using a locally computed C_{DES} in ℓ_{LES} causes the RANS region to become thinner when the mesh is fine. By maximizing the size of the eddy simulation region, the dynamic DDES model is able to reduce any drawbacks in the RANS model (such as the absence of curvature corrections while simulating rotating turbulent channel flow).

A key observation is how obvious it was to implement a dynamic procedure into our alternate DDES formulation Reddy et al. (2014). That is because it was designed to be similar to the Smagorinsky model. It is likely that other improvements/modifications made to the original Smagorinsky formulation can also be implemented. This could lead to additional robustness of this DES formulation, capable of handling a wide range of flow configurations.

The role of inflow property is also explored here. It is shown by test cases that the model naturally bridges the WMLES and nature DES applications. It is clear that using turbulence

resolved inflow condition gives better results than having RANS inflow profile.

The necessity of using turbulent resolved inflow condition is also demonstrated here. For massively separated flow, such as backward facing step, is exactly the ideal case for nature DES application. The nature DES application can produce a satisfactory result. Therefore, RANS inflow condition is good enough so that there is no need to waste computational cost for resolved, time accurate inflow condition. For moderate separation case, usually on a smooth surface, WMLES bests nature DES by better handling RANS to LES transition adjacent to the separation line. For extreme shallow separation, like the Ercoftac hill, separation bubble lines in wall model region. RANS branch can deteriorate the result. Using resolved inflow condition helps in improving the results but obviously there is a cap on accuracy.

APPENDIX. TECHNICAL SUPPLEMENTAL MATERIAL

Multi-domain for Removing Downstream Effect for LES Inlet Generation

In some test cases, recycling and rescaling of boundary layer[Arolla and Durbin (2013)] is used to generate turbulent resolved inlet profile. Boundary layer profile is taken from downstream and is imposed to inlet boundary after rescaling. Any non-homogeneous behavior of the boundary layer will be magnified by such rescaling and recycling process. For example, in that Ercoftac Hill case[4.2.2], compared to flate plate chase, upstream of the hill the pressure is changed which would influence the velocity profile. such influence magnified by recycling and rescaling will cause the boundary layer before hill to be thicker and thicker. Boudnary layer on the sides will decrease to balence the total momentum thickness due to the mechanism of that recycling method. At last, non-physical inflow condition will deteriorate the flow field.

One possible fix for that is to use two separate domains. Unlike those simulations with precursor simulation to get time varying inflow profile[Avdis et al. (2009)], this separated domain can be solved simultaneously with the main domain within single solver thanks to multi-domain handling capability in OpenFOAM[Jasak et al. (2013)].

It is shown in figure .1, the boundary condition is set to be like this: Region 1 is the separated domain to generate inflow profile while region 2 is the domain contains flow we want to solve. Inflow condition at plane A is from recycling and rescaling where the sampling plane is in region 1. Plane B is just a outflow boundary. Plane C, which is the inflow boundary of interested domain, directly uses data sampled in region 1 or plane B.

This method gives two advantages: First, the rescaling and recycling method is independent of spanwise flow non-homogeneity from downstream. Second, those two domains can be solved simultaneously to avoiding data storege and accessing problem from precursor simulation.

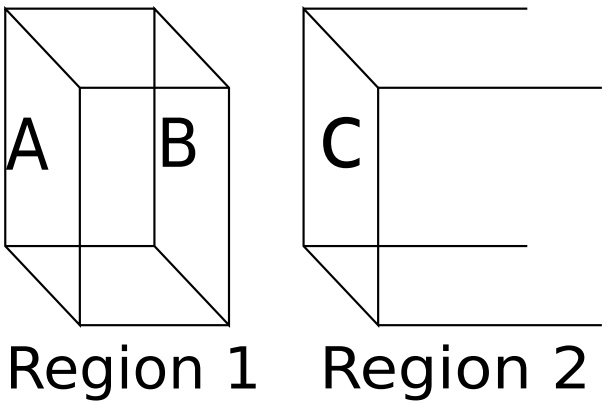

Figure .1: Sketch of multi-domain for inlet generation

BIBLIOGRAPHY

Arolla, S. K. and Durbin, P. A. (2013). Modeling rotation and curvature effects within scalar eddy viscosity model framework. *International Journal of Heat and Fluid Flow*, 39:78–89.

Arolla, S. K. and Durbin, P. A. (2014). Generating inflow turbulence for eddy simulation of turbomachinery flows. In *52nd AIAA Aerospace Sciences Meeting, National Harbor, Maryland*.

Avdis, A., Lardeau, S., and Leschziner, M. (2009). Large eddy simulation of separated flow over a two-dimensional hump with and without control by means of a synthetic slot-jet. *Flow, turbulence and combustion*, 83(3):343–370.

Baggett, J. S. (1998). On the feasibility of merging les with rans for the near-wall region of attached turbulent flows. *Annual Research Briefs*, pages 267–277.

Bardina, J., Ferziger, J. H., and Reynolds, W. (1980). Improved subgrid-scale models for large-eddy simulation. In *American Institute of Aeronautics and Astronautics, Fluid and Plasma Dynamics Conference, 13th, Snowmass, Colo., July 14-16, 1980, 10 p.*, volume 1.

Bell, J. H., Heineck, J. T., Zilliac, G., Mehta, R. D., and Long, K. R. (2012). Surface and flow field measurements on the faith hill model. *AIAA paper*.

Cherry, E. M., Elkins, C. J., and Eaton, J. K. (2008). Geometric sensitivity of three-dimensional separated flows. *International Journal of Heat and Fluid Flow*, 29:803–811.

Ducros, F., Nicoud, F., and Poinsot, T. (1998). Wall-adapting local eddy-viscosity models for simulations in complex geometries. In *International Conference on Computational Conference*, pages 293–300.

Fröhlich, J., Mellen, C. P., Rodi, W., Temmerman, L., and Leschziner, M. A. (2005). Highly resolved large-eddy simulation of separated flow in a channel with streamwise periodic constrictions. *Journal of Fluid Mechanics*, 526:19–66.

Garcia-Villalba, M., Li, N., Rodi, W., and Leschziner, M. (2009). Large-eddy simulation of separated flow over a three-dimensional axisymmetric hill. *Journal of Fluid Mechanics*, 627:55–96.

Germano, M., Piomelli, U., Moin, P., and Cabot, W. H. (1991). A dynamic subgrid-scale eddy viscosity model. *Physics of Fluids A: Fluid Dynamics (1989-1993)*, 3(7):1760–1765.

Grundestam, O., Wallin, S., and Johansson, A. V. (2008). Direct numerical simulations of rotating turbulent channel flow. *Journal of Fluid Mechanics*, 598:177–199.

Jasak, H., Jemcov, A., and Tukovic, Z. (2013). Openfoam: A c++ library for complex physics simulations.

Jeyapaul, E. (2011). *Turbulent flow separation in three-dimensional asymmetric diffusers*. PhD thesis, Iowa State University.

Kolmogorov, A. N. (1941). The local structure of turbulence in incompressible viscous fluid for very large reynolds numbers. In *Dokl. Akad. Nauk SSSR*, volume 30, pages 299–303.

Kristoffersen, R. and Andersson, H. I. (1993). Direct simulations of low-reynolds-number turbulent flow in a rotating channel. *Journal of fluid mechanics*, 256:163–197.

Launder, B. and Sharma, B. (1974). Application of the energy-dissipation model of turbulence to the calculation of flow near a spinning disc. *Letters in heat and mass transfer*, 1(2):131–137.

Lilly, D. K. (1992). A proposed modification of the germano subgrid-scale closure method. *Physics of Fluids A: Fluid Dynamics (1989-1993)*, 4(3):633–635.

Meneveau, C., Lund, T. S., and Cabot, W. H. (1996). A lagrangian dynamic subgrid-scale model of turbulence. *Journal of Fluid Mechanics*, 319:353–385.

Menter, F. and Kuntz, M. (2004). Adaptation of eddy-viscosity turbulence models to unsteady separated flow behind vehicles. In *The aerodynamics of heavy vehicles: trucks, buses, and trains*, pages 339–352. Springer.

Moser, R. D., Kim, J., and Mansour, N. N. (1999). Direct numerical simulation of turbulent channel flow up to re= 590. *Phys. Fluids*, 11(4):943–945.

Nikitin, N., Nicoud, F., Wasistho, B., Squires, K., and Spalart, P. (2000). An approach to wall modeling in large-eddy simulations. *Physics of Fluids (1994-present)*, 12(7):1629–1632.

Piomelli, U., Balaras, E., Squires, K. D., and Spalart, P. R. (2002). Zonal approaches to wall-layer models for large-eddy simulations. *AIAA Paper*, 3083.

Pope, S. B. (2000). *Turbulent flows*. Cambridge university press.

Rajamani, B. and Kim, J. (2010). A hybrid-filter approach to turbulence simulation. *Flow, turbulence and combustion*, 85(3-4):421–441.

Reddy, K., Ryon, J., and Durbin, P. (2014). A ddes model with a smagorinsky-type eddy viscosity formulation and log-layer mismatch correction. *International Journal of Heat and Fluid Flow*, 50:103–113.

Rumsey, C. (2015). 2d nasa wall-mounted hump separated flow validation case.

Seifert, A. and Pack, L. G. (2002). Active flow separation control on wall-mounted hump at high reynolds numbers. *AIAA journal*, 40(7):1363–1372.

Shur, M. L., Spalart, P. R., Strelets, M. K., and Travin, A. K. (2008). A hybrid rans-les approach with delayed-des and wall-modelled les capabilities. *International Journal of Heat and Fluid Flow*, 29(6):1638–1649.

Smagorinsky, J. (1963). General circulation experiments with the primitive equations: I. the basic experiment*. *Monthly weather review*, 91(3):99–164.

Spalart, P., Jou, W., Strelets, M., and Allmaras, S. (1997). Comments on the feasibility of les for wings, and on a hybrid rans/les approach. *Advances in DNS/LES*, 1:4–8.

Spalart, P. R. (2009). Detached-eddy simulation. *Annual Review of Fluid Mechanics*, 41:181–202.

Spalart, P. R. and Allmaras, S. R. (1992). A one-equation turbulence model for aerodynamic flows.

Spalart, P. R., Deck, S., Shur, M., Squires, K., Strelets, M. K., and Travin, A. (2006). A new version of detached-eddy simulation, resistant to ambiguous grid densities. *Theoretical and computational fluid dynamics*, 20(3):181–195.

Travin, A. K., Shur, M. L., Spalart, P. R., and Strelets, M. K. (2006). Improvement of delayed detached-eddy simulation for les with wall modelling. In *ECCOMAS CFD 2006: Proceedings of the European Conference on Computational Fluid Dynamics, Egmond aan Zee, The Netherlands, September 5-8, 2006*. Delft University of Technology; European Community on Computational Methods in Applied Sciences (ECCOMAS).

Verma, A. and Mahesh, K. (2012). A lagrangian subgrid-scale model with dynamic estimation of lagrangian time scale for large eddy simulation of complex flows. *Physics of Fluids (1994-present)*, 24(8):085101.

Visbal, M. R., Rizzetta, D. P., and Mathew, J. (2007). Large-eddy simulation of flow past a 3-d bump. *AIAA Paper*, 917:2007.

Vogel, J. C. and Eaton, J. K. (1985). Combined heat transfer and fluid dynamic measurements downstream of a backward-facing step. *Journal of Heat and Mass Transfer*, 107:922–929.

Walters, D., Bhushan, S., Alam, M., and Thompson, D. (2013). Investigation of a dynamic hybrid rans/les modelling methodology for finite-volume cfd simulations. *Flow, turbulence and combustion*, 91(3):643–667.

Wilcox, D. C. (1993). *Turbulence Modeling for CFD*. DCW Industries.